KTH Electrical Engineering

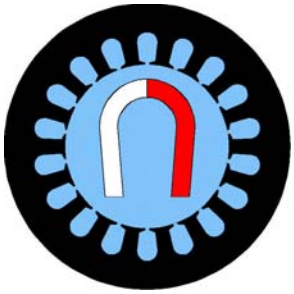

Permanent Magnet Drives

Design and optimization of a surface-mounted permanent magnet synchronous motor for a high cycle industrial cutter

by

Alexander Stening

Master Thesis

Supervisors:
Dr. Juliette Soulard
Tech. Lic. Florence Libert

Royal Institute of Technology
Department of Electrical Engineering
Electrical Machines and Power Electronics

Stockholm March 2006
XR-EE-EME 2006:002

Abstract

In this master thesis, a surface-mounted permanent magnet synchronous motor is designed and optimized analytically. The motor is supposed to be used in a high cycle industrial cutter. Due to the application, there is a limited amount of space for the motor which set constraints on the design. The motor should be optimized for a rated torque of 5,5 Nm at a speed of 10 000 rpm.

An analytical design method for surface mounted permanent magnet motors is described. Analytical models are developed taking the motor losses into account. Special attention is given to the thermal properties of the machine. A thermal model used to predict the temperature distribution in the machine is presented. Mechanical restrictions regarding the magnet fixation are also considered.

The first part of the thesis consists of a literature review in order to build the required knowledge of the topic. Based on this theory, the different models required for the design work was developed. In order to find a suitable design, the machine performance was studied for different machine geometries. The main concern was to find a machine design that resulted in a low amount of copper losses. Thus, a low operating temperature was achieved.

The thesis resulted in a suggested machine design. This design was studied with finite element method in order to verify the analytical results. A comparison was made between the two methods and the results showed acceptable correlation, leading to the fulfilment of the requirements.

Acknowledgements

This master thesis was written at the Department of Electrical Engineering, division of Electrical Machines and Power Electronics, Royal Institute of Technology, Stockholm. The thesis was performed in cooperation with Electrolux AB, Jonsered.

A special thank goes to my supervisors Dr. Juliette Soulard and Tech. Lic. Florence Libert for all the assistance during my work. I am also very grateful to Ulf Petersson from Electrolux who made this thesis work possible. And I would also like to thank the rest of the staff at Jonsered for the interesting field trip in October 2005.

I would like to thank all the personal of EME for helping me in any way. It has been a pleasure to work here.

Finally I would like to thank Jan Timmerman for his invention of the storkvagn which has increased his stork delivery capacity. The Roebel´s bar was always a pleasure, especially the Torsk-Roebel evenings.

Contents

1 Introduction

Electrical motors have been widely used in industrial applications for a very long time. The electric power production is almost exclusively formed by synchronous machines. While the robust induction machines are the most common machine types in industrial applications. The use of permanent magnet materials in electrical machines have been known for a long time. But due to the low energy product of the ferrite materials used at that time the use was limited to low power machines. However, frequency converters and new materials bring new possibilities for the machine designers. New permanent magnet materials with high energy product have been commercially developed since the 1970´s. This started a large-scale development of the permanent magnet synchronous machines. High efficiency and accurate control of the machines are demands that are more and more important in industrial applications. A permanent magnet motor and a frequency converter together form a concept well-suited for variable speed drives. The permanent magnet synchronous machine (PMSM) is essentially a synchronous machine where the excitation winding is replaced with permanent magnets. Thus the PMSM has negligible rotor losses. Of course this gives an improved efficiency, but it will also give a lower operating temperature of the machine. The temperature is the limiting factor when it comes to the maximum possible output power of the machine. Therefore, the permanent magnet motors have an outstanding power to weight ratio. Further on, they offer an improved power factor relatively independent of the pole number and speed.

1.1 Presentation of the thesis

This thesis has been performed in cooperation with Electrolux AB. The objective is to design a permanent magnet motor to drive an industrial hand grinder. The main part of the thesis consists of the development of different models needed during the analytical design work. Different losses as well as mechanical dimensioning and thermal properties are considered. Special attention is given to the thermal modelling to be able to increase the power density of the machine. The developed models are then used during the design process in order to find an optimal machine design. Finite element method is also used for verification of the results obtained for the final analytical design. This design will hopefully result in a prototype machine. But this is beyond the scope of this thesis.

1.1.1 Specifications

The machine design is based on the specifications from Electrolux. In the application, there is a certain space available for the motor. This restriction results in a high value required for the power density. Therefore, the choice of a permanent magnet machine is probably the only solution. The specifications are listed in Table 1-1.

Motor type	Inner rotor PMSM
Cooling	Water cooled
Number of phases	3
Rated speed	≈ 10000 rpm
Rated torque	≈ 5,5 Nm
Outer diameter	≤ 110 mm
Total length	≤ 80 mm
Total mass	≤ 4,5 kg
Drive	Sinus PWM

Table 1-1 Motor specifications

The stator frame with cooling ducts is supposed to be included within the maximum outer diameter. The total length is supposed to include the shaft bearings. The drive (power electronics + control) is not integrated in the hand grinder. The power electronics is placed in a separate box with its own cooling system. The total mass refers to the motor itself.

2 Literature study

In this chapter, the literature review is summarized. The basic theory of magnetic materials is presented and the most commonly permanent magnet materials are introduced. Different concepts of radial-flux permanent magnet synchronous machines are presented. Different bandage materials are introduced and theory regarding the minimum required bandage thickness is also presented. The different losses in a PMSM machine are introduced and some general theories regarding these losses are given. An introduction to heat transfer theory is also made.

2.1 Magnetic materials

Ferromagnetic materials can be divided into soft and hard magnetic materials. This is depending on the magnitude of the magnetic field strength H that is required to saturate the material. The soft magnetic materials can be described by their relative permeability μ_r. The relative permeability is a measure of how easy the material can be magnetized by an external field H. The magnetic flux density B in the material is given by:

$$B = \mu_0 \mu_r H \tag{2-1}$$

where μ_0 is the permeability of free space. For a soft magnetic material μ_r is high and the magnetic field strength required for saturation is low. This means that the area enclosed by the hysteresis loop is small and thus the hysteresis losses are low. This makes a soft magnetic material suitable as lamination in electrical machines where the lamination is used to complete the flux path.

2.1.1 Properties of permanent magnet materials

Permanent magnet materials used to create an airgap flux in electrical machines are hard magnetic materials. They have a low relative permeability ($\mu_r \approx 1$) and require a high magnetic field strength for saturation, but they then keep this magnetisation.
Permanent magnet materials are usually graded by their maximum energy product $(BH)_{\max}$.
This is twice the maximum energy that can be stored within a permanent magnet material in the absence of any externally applied field. The magnet with the highest energy product will have the smallest volume for producing a specific flux density. The remanence flux density B_r is a measure of the materials magnetization without any external field. A high remanence flux density is required in order to obtain a high energy product. The flux density within a permanent magnet can be expressed by the following idealized expression [1]:

$$B = B_r + \mu_0 \mu_r H \tag{2-2}$$

Another important quality is the materials coercivity H_{cJ}. It is a measure of the reverse field needed to drive the magnetization to zero after being saturated. A high coercivity means that the magnet can sustain a high demagnetization field.

The remanence flux density is temperature dependent, it will decrease for increased temperatures. Normally the remanence is given in reference to 25° C.

$$B_r = B_r(25^o\,C)\cdot(1+\alpha_{B_r}\Delta T) \qquad \textbf{(2-3)}$$

where α_{B_r} (< 0) is the reversible temperature coefficient and ΔT is the deviation from the reference temperature. Thus it is important to know the magnets operating temperature. Further on, the coercivity is also decreasing for an increased temperature. Thus the permanent magnets can be more easily demagnetised when they are warm. It is possible to assign an approximately constant value to the reversible temperature coefficient of B_r. But the reversible temperature coefficient of H_{cJ} is not as easy to predict. Instead, the actual demagnetization curves can be used to study this parameter.

2.1.2 Samarium Cobalt magnets

Samarium cobalt magnets, SmCo has been mostly used in electrical machines before the introduction of the NdFeB-magnets. SmCo-magnets can resist a very high operating temperature and have good temperature stability over a large temperature range. Due to its temperature stability, the material is very suitable in sensor applications. The material can also be suitable in electrical machines if the operating temperature is very high. But the SmCo-magnets are very brittle and quite expensive, approximately 20-30 % more expensive then NdFeB-magnets [1]. Characteristics of the SmCo-magnets are [1]:

- relatively high remanence, $B_r \le 1{,}15$ T
- reversible temp. coeff. of B_r, 20-150 °C, $-0{,}045 \le \alpha_{B_r} \le -0{,}035$ % K^{-1}
- good energy density, $(BH)_{\max} \le 240\ kJ/m^3$
- high temperature stability, up to 350° C (continuously)
- high Curie temperature, approximately up to 800° C
- high coercivity, $H_{cJ} < 2400\ kA/m$

2.1.3 Neodymium Iron Boron magnets

Neodymium iron boron, NdFeB is the most commonly used material in high power density permanent magnet machines. This is due to its high energy product which reduce the magnet volume required for a specific airgap flux density. NdFeB-magnets have a high remanence flux density and a high coercivity at relatively high temperatures. But they have a low Curie temperature and are not as temperature stable as the SmCo-magnets are. NdFeB is also more sensitive to humidity than SmCo and should therefore be coated with a protection layer. Characteristics of the NdFeB-magnets are [1]:

- high remanence, $B_r \le 1{,}4$ T
- reversible temp. coeff. of B_r, 20-150 °C, $-0{,}12 \le \alpha_{B_r} \le -0{,}11$ % K^{-1}
- high energy density, $(BH)_{\max} \le 385\ kJ/m^3$
- good temperature stability, up to 200° C (continuously)
- low Curie temperature, approximately up to 350° C
- high coercivity, $H_{cJ} < 3260\ kA/m$

2.2 Radial-flux inner rotor PM synchronous machines

In radial-flux machines, the flux through the airgap flows in the radial direction while the current flows in the axial direction. This gives a resulting force on the rotor acting in the tangential direction. Radial-flux synchronous machines with inner rotor are the most commonly used permanent magnet machines. Other concepts of PM machines are also used, such as axial-flux machines and radial-flux machines with outer rotor. But these machines are not treated in this thesis.
Radial-flux PM machines can be designed in several ways with different stator windings and different rotor configurations. The most commonly rotor configurations of inner rotor PM machines are presented in this section. More information about different PM machine concepts can be found in [3].

2.2.1 Surface-mounted PM machines

Surface mounted permanent magnets (SMPM) is the most common rotor configuration for PM machines. The magnets are placed on the rotor surface as shown in Figure 2-1.

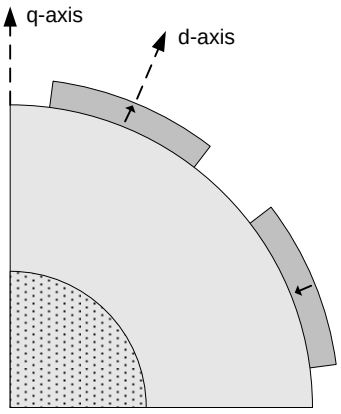

Figure 2-1
Cross section of a quarter of an 8-pole rotor with surface mounted magnets

The magnets are glued onto the rotor surface and fixed by a carbon or glass fibre bandage. In relation to other PM concepts, the surface mounted machines are easy to manufacture and consequently the construction cost is lower. The main drawback of these machines is the exposition of the permanent magnets to demagnetisation fields. The magnets are also subject to high centrifugal forces. But at moderate peripheral speeds, the use of a glass fibre bandage is usually enough to withstand these forces. As the permeability of the magnets is almost the same as the permeability of air, the d-axis and the q-axis reluctances are equal. Hence, the SMPM machines have no saliency and the torque is produced by the interaction between the stator currents and the magnets only.

2.2.2 Inset PM machines

In inset PM machines, the magnets are mounted on the rotor surface as shown in Figure 2-2. But the magnets are sunken in the rotor core, offering better protection than in a SMPM machine. However, a bandage is often required in order to withstand the centrifugal forces. Due to the iron between the magnets, the q-axis reluctance is lower than the d-axis reluctance. This is known as salient poles. Due to the saliency, a reluctance torque is created in addition to the torque from the magnets.

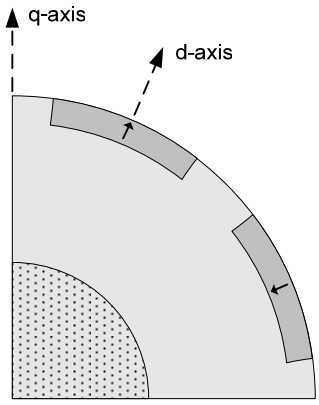

Figure 2-2
Cross section of a quarter of an 8-pole rotor with inset magnets

2.2.3 Buried PM machines

Another PM concept is to bury the magnets in the rotor core as shown in Figure 2-3. This is referred to as buried PM machines. The magnets are better protected against demagnetisation fields and mechanical stress. There are many different possibilities for the placement of magnets in the rotor. The magnets can be placed in such a way that the flux generated by the magnets in the rotor is concentrated and thus high airgap flux densities can be achieved [3]. As the inset PM machines the buried PM machines have salient poles. A main drawback of the buried PM machines is the difficult manufacturing process and thus the high production cost.

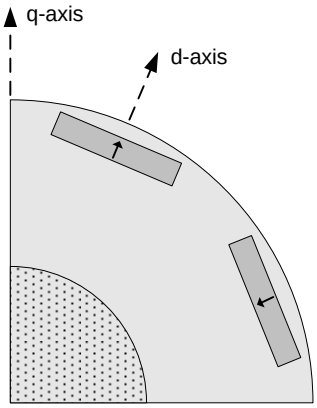

Figure 2-3
Cross section of a quarter of an 8-pole rotor with buried magnets

2.3 Bandage

The machine design is influenced by mechanical restrictions of the fixation of the rotor magnets due to high speed operation. When the magnets are exposed to high mechanical stress, a carbon or glass-fiber bandage is required in order to withstand these forces. Another possible solution is to use a non-magnetic steel cylinder to cover the magnets. The steel cylinder is very strong but flux variations will cause eddy currents resulting in larger losses compared to the composite bandage. Figure 2-4 shows a cross section of a 4-pole surface mounted PM rotor with bandage (the bandage is usually not as thick as shown on the figure).

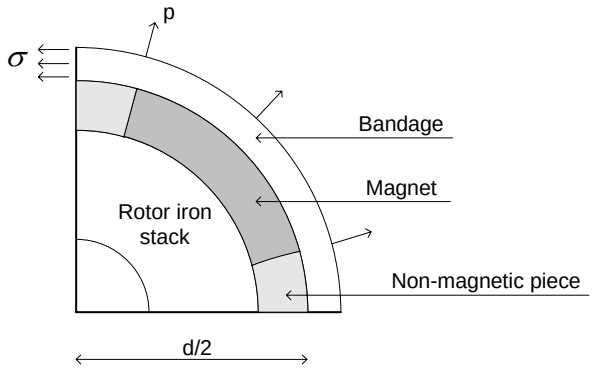

Figure 2-4 A quarter of a SMPM rotor with bandage

The total gap between the rotor outer diameter and the stator core consists of the magnet height, the bandage thickness and the mechanical airgap. A large magnet height requires a thicker bandage than a thinner magnet. This leads to a larger total magnetic airgap. Therefore the output power of the machine is directly influenced by the mechanical restrictions of the magnet fixation. The next section presents the method used to determine the minimum composite bandage thickness [2].

2.3.1 Minimum bandage thickness

The modulus of elasticity in tension, also known as Young's modulus E, is the ratio of stress to strain on the loading plane along the loading direction.
The minimum Young's modulus E_B of a bandage consisting of 60% glass-fiber and 40% epoxy, is given as : $E_B = 42000\,N/mm^2$.
The inner diameter of the prefabricated glass fiber bandage cylinder is smaller than the rotor outer diameter d, by the value Δd. After pressing the bandage on the rotor, the initial tangential tension within the bandage is given by :

$$\sigma = \frac{\Delta d}{d} E_B \qquad \textbf{(2-4)}$$

The pressure of the bandage on the magnets can be written as:

$$p_{bm} = \frac{2\sigma h_b}{d + h_b} \qquad \textbf{(2-5)}$$

where h_b is the bandage thickness. The centrifugal pressure p_{mb} of the magnets on the bandage is calculated for an over-speed ω_{over} of 120% the nominal mechanical angular velocity ω_m, which gives :

$$p_{mb} = r_m \rho_m (2\pi\omega_{over})^2 h_m \quad \textbf{(2-6)}$$

Where r_m is the average radius of the magnets, ρ_m is the mass density of the magnet material and h_m is the height of the magnets.
The centrifugal pressure p_{bb} of the bandage is calculated using Equation (2.6), replacing the average radius r_m by the average radius of the bandage r_b, ρ_m by the mass density of the bandage ρ_b and the height h_m by the height of the bandage h_b.

$$p_{bb} = r_b \rho_b (2\pi\omega_{over})^2 h_b \quad \textbf{(2-7)}$$

The residual pressure p_{res} is calculated as the difference between the pressure of the bandage and the sum of the centrifugal pressure of the magnets and the bandage. In order to ensure that the magnets are fixed on to the rotor surface, the residual pressure must be larger than zero.

$$p_{res} = p_{bm} - p_{mb} - p_{bb} > 0 \ N/mm^2 \quad \textbf{(2-8)}$$

A second condition guarantees that the bandage does not burst. The maximum tangential strength must be lower than 600 N/mm^2, which is the limit for glass fiber-epoxy prefabricated bandage shells at a temperature of 150° C. The maximum tangential strength $\sigma_{\max}$ is calculated from the initial strength σ as follows:

$$\sigma_{\max} = \sigma \frac{p_{bm} + p_{mb} + p_{bb}}{p_{bm}} < 600 \ N/mm^2 \quad \textbf{(2-9)}$$

Both Equation (2-8) and Equation (2-9) have to be fulfilled to ensure that the bandage is strong enough.

2.4 Losses in surface-mounted permanent magnet machines

In this section, the different losses in a SMPM machine are introduced and general theory is given. The exact loss models used in this thesis are presented in chapter 5.
The main losses in a SMPM machine are copper losses and iron losses but there are also mechanical losses. The mechanical losses are often small in relation to the electrical losses. But the bearing losses and the windage losses may be important if the rotational speed is high.

2.4.1 Copper losses

The copper losses often form the largest fraction of the total losses in a PMSM machine. The copper losses are calculated as follows:

$$P_{cu} = 3R_{cu}I^2 \tag{2-10}$$

where R_{cu} is the winding resistance of one phase and I is the rms-value of the stator current. The winding resistance is depending on the conductor area and length, i.e. the number of conductors per slot n_s and the slot area A_{sl}. The slot fill factor f_s is an important parameter when determining the copper losses. The slot fill factor is the ratio between the copper area and the slot area. Consequently a high fill factor reduces the copper losses. The winding resistance of one phase is calculated as [3]:

$$R_{cu} = \rho_{cu}\frac{\left(pL + (D + h_{ss})\pi k_{coil}\right)n_s^2 q}{f_s A_{sl}} \tag{2-11}$$

where ρ_{cu} at the given temperature of the winding is the resistivity of copper, p the number of poles, L the active length of the machine, D the inner stator diameter, h_{ss} the slot height and q the number of slots per pole and phase. The End-windings are taken into account by introducing the term $D\pi k_{coil}$ [3], where k_{coil} is an empirical constant depending on the winding arrangement.

2.4.2 Iron losses

Iron losses are due to the variation of the flux density in electromagnetic material. The flux variations create eddy currents and magnetic hysteresis in the iron laminations of motors. The hysteresis loss is depending on the peak value and the frequency of the flux density. The eddy current loss is depending on the time rate of change of the flux density [4]. The iron losses can form a significant fraction of the total loss. This is partly due to the high value of the flux density in the stator core to save place for the winding. Predicting these losses with accuracy is a complex task but an estimation can be done rather easily. An analytical model that can be used to estimate the iron losses in the stator core of a surface mounted PMSM is presented in this section.

The iron losses in the rotor are more complicated to evaluate analytically as they are created by the time and space harmonics of the total rotating flux in the airgap. The flux density in the rotor core is mainly constant so the rotor losses are of minor importance. Usually time-step finite element methods are used in order to evaluate the rotor core losses. This method is described further in chapter 5 and results are presented in chapter 7.

Standards define that the measurements of iron losses in magnetic material are made with a sinusoidal flux density of varying frequency and magnitude (Epstein frame test). The total iron loss density $\mathrm{p}_{\mathrm{iron}}$ is commonly expressed in the following form for a sinusoidal flux density of amplitude $\hat{B}$ with angular frequency ω_e:

$$p_{iron} = p_h + p_e = k_h \hat{B}^{\beta_{St}}\omega_e + k_e \hat{B}^2 \omega_e^2 \tag{2-12}$$

where p_h and p_e are the hysteresis and the eddy current loss density respectively, k_h and k_e are hysteresis and eddy current constants and β_{St} is the Steinmetz constant. All constants depend on the iron lamination material. Typical values for grades of silicone iron laminations used in small and medium machines are in the ranges of:
k_h = 40-55 [Ws/T^2/m^3], β_{St} = 1,8-2,0 and k_e = 0,04-0,07 [Ws^2/T^2/m^3] [4].
Notice that Equation (2-12) is valid only for sinusoidal flux density.

In a SMPM machine, the flux density in the stator core may be far from sinusoidal, hence the iron loss density has to be evaluated by a more complicated model. The hysteresis loss is still relatively easy to evaluate as it only depends on the peak value of the flux density and the frequency of the fundamental of the variations.

In the analytical model, the stator core is divided into two parts: the stator teeth and the stator yoke. p_{teeth} and p_{yoke} are the loss density in each area defined as the sum of the hysteresis and the eddy current loss density.

$$p_{teeth} = p_{h\_teeth} + p_{e\_teeth} \quad \textbf{(2-13)}$$

$$p_{yoke} = p_{h\_yoke} + p_{e\_yoke} \quad \textbf{(2-14)}$$

Assuming that there are no minor hysteresis loops, the hysteresis loss density can be calculated as:

$$p_{h\_teeth} = k_h \hat{B}_{st}^{\beta_{St}} \omega_e \quad \textbf{(2-15)}$$

$$p_{h\_yoke} = k_h \hat{B}_{sy}^{\beta_{St}} \omega_e \quad \textbf{(2-16)}$$

where $\hat{B}_{st}$ and $\hat{B}_{sy}$ are the maximum flux density in the stator teeth and the stator yoke respectively.

When the flux density is non-sinusoidal, the eddy current loss becomes quite difficult to calculate. Expressions for the teeth and the yoke eddy current loss densities can be found in [4]. These equations are based on comparisons with a finite element method and take into account both the radial and circumferential flux density components. A modified expression for the eddy current loss density in the stator teeth is:

$$p_{e\_teeth} = \frac{12}{\pi^2} q k_q k_c k_e (\omega_e B_{st})^2 \quad \textbf{(2-17)}$$

where q is the number of slots per pole and phase, k_c and k_q are geometry dependent correction factors that can be found in Figure 2-5 and Figure 2-6 respectively.

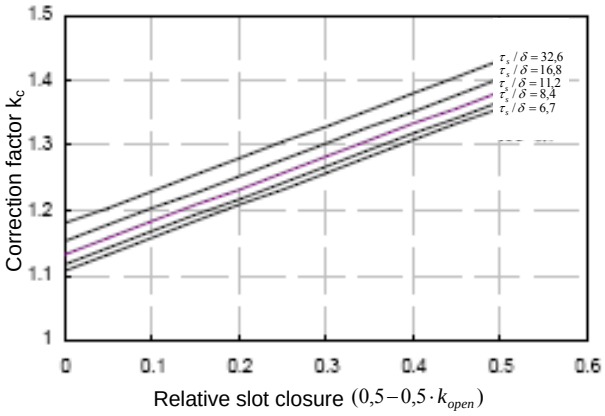

Figure 2-5 Determination of k_c [5]

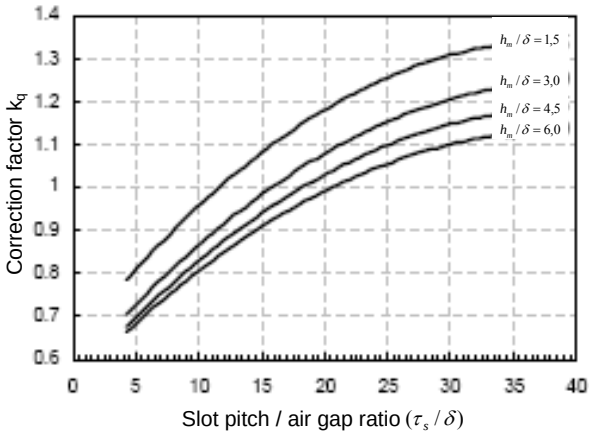

Figure 2-6 Determination of k_q [5]

For the stator yoke, the power loss density becomes:

$$p_{e\_yoke} = \frac{1}{\mathrm{cov}}\frac{8}{\pi^2}k_e\omega_e^2\hat{B}_{sy}^2\left(1+\frac{8k_q h_{sy}^2}{27\,\mathrm{cov}\,q\,\tau_{s2}^2}\right) \quad \textbf{(2-18)}$$

where *cov* is the magnet coverage in percentage of the rotor core pole pair circumference:

$$\mathrm{cov} = \frac{2\alpha}{\pi} \quad \textbf{(2-19)}$$

τ_{s2} is the projected slot pitch at the middle of the yoke. 2α is the pole angle given in electrical rad.

The total iron loss in the stator core with a non-sinusoidal flux density distribution can now be determined using the modified loss model derived from Equation (2-13) and Equation (2-14).

$$P_{loss\_stator} = V_{teeth}\,p_{teeth} + V_{yoke}\,p_{yoke} \quad \textbf{(2-20)}$$

Where V_{teeth} and V_{yoke} is the total volume of the teeth and the yoke respectively.

2.4.3 Windage losses

Windage losses are due to friction between the air and the rotor surface. If the rotor surface area is small, these losses are negligible at moderate rotational speeds. For the machine treated in this thesis, the rotational speed has to exceed approximately 30 000 rpm in order to get a noteworthy amount of windage losses. This is due to the small rotor surface. In this section, an expression for the friction torque of an enclosed rotating cylinder is derived [5].

Friction losses are set by the velocity field and the gas properties. The velocity profile in the airgap of an electrical machine is depending on the following flows:

- Tangential flow due to the rotor rotation
- Axial flow of the cooling gas through the airgap
- Taylor vortices due to centrifugal forces.

Each flow is more or less important depending on the machine dimensions, its rotational speed and the physical properties of the airgap medium. The nature of a gas flow is determined by the Reynolds number. The Reynolds number is calculated in different ways depending on the geometry. For an enclosed rotating cylinder without forced axial flow, the turbulence in the airgap is described by the Couette-Reynolds number Re_δ.

$$\mathrm{Re}_\delta = \frac{\rho v_r \delta}{\mu} \tag{2-21}$$

Were ρ is the density and μ the dynamic viscosity of the gas, v_r is the peripheral speed of the rotor and δ is the radial mechanical airgap length.

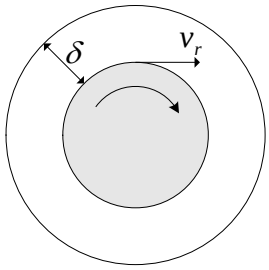

Figure 2-7: Enclosed rotating cylinder

If the Reynolds number is below 2000, the flow is characterised as laminar. In a laminar tangential flow all the particles are flowing in the same direction and the velocity distribution is linear. If the rotor speed is increased, the Reynolds number increases and the particles are no longer flowing in the same direction, although one mean direction can be determined. This kind of flow is turbulent. The turbulent flow appears at lower velocity if there is surface roughness. In electrical machines the flow is usually turbulent.
The fluid velocity near the rotor surface is the same as the surface speed of the rotor and the speed near the stator surface is zero.

The rotating cylinder in Figure 2-7 is giving rise to a tangential flow which is either laminar, Figure 2-8, or turbulent, Figure 2-9.

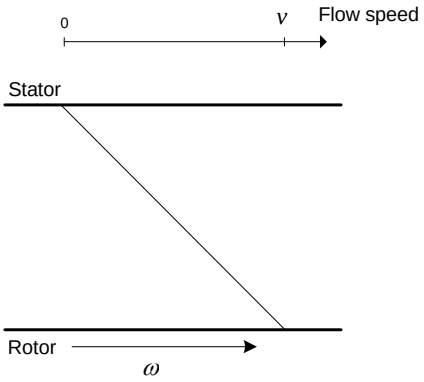

Figure 2-8 Laminar flow

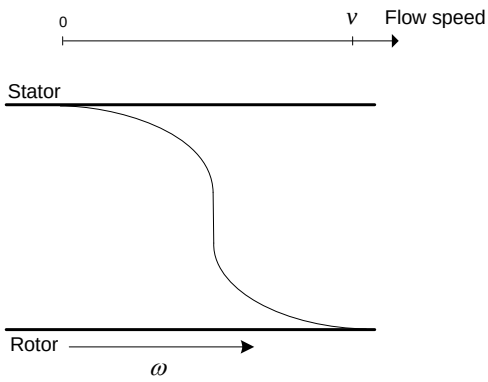

Figure 2-9 Turbulent flow

The turbulent flow can be separated into three different layers, two viscous layers near the stator and rotor walls, and one fully turbulent layer in the middle of the flow. In the viscous

layers the friction is mainly determined by the molecular viscosity of the airgap medium, but in the fully turbulent layer the particle motion is independent of viscosity.
If the rotational speed is high, the centrifugal force can affect the particles in such a way that it gives rise to Taylor vortices. Taylor vortices are circular velocity fluctuations in the airgap, figure 2-10.

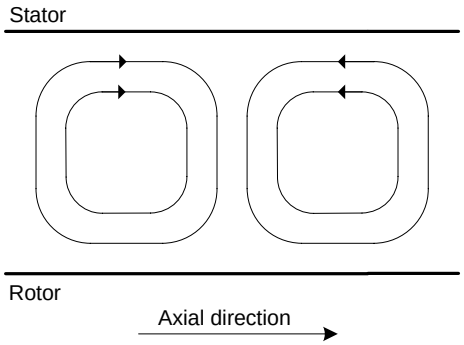

Figure 2-10: Taylor vortices

At low rotational speeds, the flow is usually laminar and the Taylor vortices are damped by frictional forces. However, these velocity fluctuations depend on the radial length of the airgap which is included in the Taylor number given by:

$$Ta = \mathrm{Re}_\delta^2 \frac{\delta}{r_r} = \frac{\rho^2 \omega_m{}^2 r_r \delta^3}{\mu^2} \qquad \textbf{(2-22)}$$

Where ω_m is the angular velocity of the rotor. The radius of the rotor r_r should be replaced with the mean airgap radius. Taylor vortices occur when the Taylor number exceeds 1700, this is called the critical Taylor number. If the speed is increased further the Taylor vortices disappear. This is supposed to happen when the Reynolds number Re_δ exceeds $5 \cdot 10^4$.

As the nature of the turbulent flow is complex the frictional stress is difficult to analyse. This is usually done using an empirical dimensionless friction coefficient C_f. If neglecting the effect of the rotor end surfaces, the shear stress in $\mathrm{N/m}^2$ on the rotor surface can then be written as:

$$\tau_r = \frac{1}{2} C_f \rho v_r^2 \qquad \textbf{(2-23)}$$

The tangential friction force acting on the rotor surface becomes:

$$F_r = \tau_r 2\pi r_r L = C_f \rho v_r^2 \pi r_r L = C_f \rho \omega_m^2 \pi r_r^3 L \qquad \textbf{(2-24)}$$

Where L is the length of the rotating cylinder, i.e. the active length of the machine.
This force is balanced by the electromagnetic torque acting on the rotor, hence it contributes to the machine losses. The friction torque is defined as:

$$T_{f_r} = F_r r_r = C_f \rho \omega_m^2 \pi r_r^4 L \qquad \textbf{(2-25)}$$

The power loss is depending on the roughness of the surfaces. This is taken into account when introducing the roughness coefficient k_f, which for smooth surfaces is equal to1,0.

The power loss due to friction in the airgap is then given as:

$$P_{f_r} = k_f T_{f_r} \omega_m \tag{2-26}$$

Using Eq. (2-26) combined with Eq. (2-25) results in:

$$P_{f_r} = k_f C_f \rho \omega_m^3 \pi r_r^4 L \tag{2-27}$$

The friction coefficient is depending on many factors and it is often empirically determined. Bilgen and Boulos (1973) made measurements on friction torque of enclosed smooth cylinders and developed equations for the friction coefficient. For turbulent flow, the friction coefficient is given as:

$$C_f = 0{,}515 \frac{\left(\frac{\delta}{r_r}\right)^{0,3}}{\mathrm{Re}_\delta^{0,5}} \quad \text{for} \quad 500 < \mathrm{Re}_\delta < 10^4 \tag{2-28a}$$

$$C_f = 0{,}0325 \frac{\left(\frac{\delta}{r_r}\right)^{0,3}}{\mathrm{Re}_\delta^{0,2}} \quad \text{for} \quad 10^4 < \mathrm{Re}_\delta \tag{2-28b}$$

The effect of Taylor vortices are modelled with the ratio of the airgap length to the rotor radius. The experimental friction coefficients deviated less than 8,35 % from the results calculated by the Equations (2-28) [5].

Juha Saari made some measurements of the roughness factor on a high speed air cooled induction motor. One aim of the experiment was to study if the surface roughness caused by the stator slot openings affects the friction losses in the airgap. Friction losses were measured using two different stator constructions, one stator with groves due to the depth of the slot opening, and one stator where these groves were filled with industrial cement in order to give a smoother surface. However, the results showed that the friction losses slightly decreased when using the stator with filled slots, but the difference was marginal.
Based on the measured losses, Saari calculated the roughness coefficient k_f. At rotational speeds of 600-1100 m/s, the roughness coefficient became 1,25 with "open" stator slots, corresponding to 1,13 with filled stator slots.
More detailed information about the experiment can be found in [5].

2.4.4 Bearing losses

The bearing losses are depending on a lot of factors, such as bearing type, lubrication, shaft load and rotor speed. The friction torque of a bearing is quite complex to calculate if high accuracy is required, but for an estimation it can be done rather easily. In literature, different formulas can be found of varying complexity, for example in [1, 6].
Under normal operating conditions and when the bearing load is about 10 % of the basic dynamic load rating, assuming the lubrication is good, the frictional torque can be estimated as [1]:

$$T_{f_b} = \frac{1}{2} \mu_f F_b d_i \tag{2-29}$$

where F_b is the radial bearing load, d_i is the inner diameter of the bearing and μ_f is the coefficient of friction for the bearing. The coefficient of friction is depending on the bearing type and can be found in [7], typically in the range of $1{,}0 \cdot 10^{-3} - 5{,}0 \cdot 10^{-3}$. A more accurate equation is obtained if the friction torque is separated into two terms, one load independent part T_0 and one load dependent part T_1 [8].

$$T_{f_b} = T_0 + T_1 \tag{2-30}$$

The equations for T_0 and T_1 are depending on the bearing type as well as the operating conditions, more information can be found in [6, 7, 8].

2.5 Heat transfer theory

Whenever a temperature gradient exists within a system, energy is transferred. This process is known as heat transfer, by which the internal energy of a system is changed. The first law of thermodynamics states that energy can neither be created nor destroyed but only changes from one form to another. But this implies no restriction on the direction of the transformation. The second law of thermodynamics states that heat must flow in the direction from higher to lower temperature. All heat transfer processes obey the first as well as the second law of thermodynamics.
Heat can be transferred in three different forms: conduction, convection and radiation. Basic principles for each form of heat transfer are presented below. More detailed information can be found in [9].

2.5.1 Conduction

If a temperature gradient exists in a solid medium, heat will flow from the higher temperature region to the lower temperature region. The rate at which heat is transferred by conduction, or the heat flow q_k [W], through a one-dimensional plane geometry with area *A*, is defined by *Fourier's Law* as [9]:

$$q_k = -k_k A \frac{dT}{dx} \tag{2-31}$$

where *T(x)* is the local temperature, *x* the distance in the direction of the heat flow and k_k is the thermal conductivity of the medium. The minus sign is a consequence of the second law of thermodynamics. For a simple case of steady-state heat flow through a plane wall, the temperature gradient and the heat flow do not vary with time and the cross-sectional area along the heat flow path is uniform. And if the thermal conductivity is independent of the temperature, Equation (2-31) can be written as:

$$q_k = \frac{Ak_k}{x}\left(T_{hot} - T_{cold}\right) \tag{2-32}$$

The thermal resistance that the wall offers to the flow of heat by conduction is given by:

$$R_k = \frac{x}{Ak_k} \tag{2-33}$$

Most parts in an electrical machine are usually modelled with thermal conduction equivalent resistances.

2.5.2 Convection

If a temperature gradient exists on the surface between a body and a surrounding medium (fluid), heat is transferred by convection. The heat transfer consists of two mechanisms operating simultaneously: heat conduction and mechanical fluid motion. The fluid motion is caused by an external force. Depending on the nature of the external force, convection is classified as forced or natural. In forced convection, the external force is due to a pressure

difference generated by a pump or a fan. In natural convection, a gradient of fluid density produces an external force. The convective heat transfer coefficient h_c, depends on the density, viscosity, flow characteristics and velocity of the fluid as well as on its thermal properties. These quantities are not necessarily constant over a surface. Therefore the average value of the convective heat transfer coefficient $\bar{h}_c$, is often used in engineering applications. The heat flow by convection can be calculated from *Newton's Law of Cooling* [9]

$$q_c = \bar{h}_c A \Delta T \tag{2-34}$$

where ΔT is the difference between the surface temperature and the temperature of the fluid. The average heat transfer coefficient $\bar{h}_c$ is calculated over the heat flow area *A*.
The thermal equivalent resistance to convective heat transfer is defined as:

$$R_c = \frac{1}{\bar{h}_c A} \tag{2-35}$$

Evaluation of $\bar{h}_c$ is difficult as N*ewton's Law of Cooling* is rather a definition of $\bar{h}_c$ than a law of convection.
In an electrical machine, the surface between the stator frame and the cooling medium is an area where convective heat transfer occurs as well as in the airgap.

2.5.3 Radiation

The amount of energy leaving a surface as radiant heat depends on the temperature and the nature of the surface. The heat flow emitted by a body with area A, and at temperature T_s, to the surroundings at temperature T^{∞} is given by *Stefan Boltzmann's Law* [9].

$$q_r = k_B \varepsilon A\left(T_s^4 - T_\infty^4\right) \tag{2-36}$$

The body is assumed to be enclosed by a blackbody, i.e. all radiant heat is absorbed by the enclosure. k_B is the Stefan Boltzmann constant equal to $5{,}67 \cdot 10^{-8}$ [W/m^2/K^4], and ε is the emittance of the body's surface ($\varepsilon \leq 1$).

One can see that it requires a large area or a large temperature difference in order to get a noteworthy amount of radiant heat transfer. In a machine, this is usually not the case. Therefore the amount of power transferred by radiation is usually neglected.

3 The motor drive

The permanent magnet synchronous motor requires power electronics in order to start and operate at variable speed. The rotational speed is proportional to the frequency of the input voltage, therefore the motor has to be supplied with a voltage of variable frequency. This is done with power electronics. This chapter presents a basic design of a motor drive that can be used for the application. The output voltage of the drive that is applied to the motor u_{LL} is calculated. This result is used further during the machine design process.

3.1 Overview of the drive system

A simple drive solution that satisfies the demands is shown in Figure 3-1.

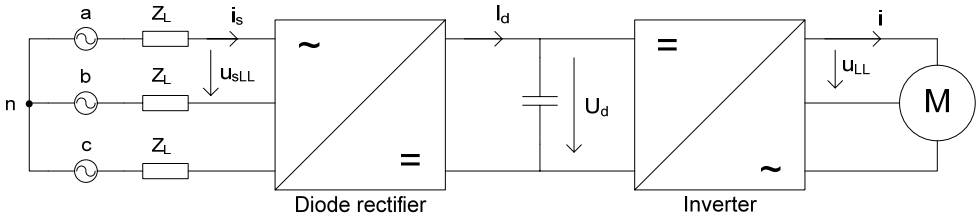

Figure 3-4: Basic drive system

The drive system consists of two main parts, a three phase diode rectifier and a three phase inverter. These parts are coupled via a smoothing capacitor. The grid connection can be modeled with the impedance:

$$Z_L = R_L + jX_L \tag{3-1}$$

This section presents general theory regarding the main components in the drive system.

3.1.1 Line and cable impedance

The main grid is assumed to be strong, therefore the magnitude of the phase voltages u_a, u_b and u_c are independent of the size of the load. Further on, the cable connecting the inverter and the motor is assumed to be short and well suited for the application, for that reason it will not affect the output voltage significantly and the impedance can be neglected. More information regarding the grid connection is required in order to model the impedance Z_L. Therefore the impedance Z_L is treated as small.

3.1.2 Rectifier

For an ideal three-phase diode rectifier, the average value U_{d0} of the rectified voltage u_d depends on the rms value of the input line to line voltage U_{sLL} as [10]:

$$U_{d0} = \frac{1}{T}\int_0^T u_d dt = \frac{3\sqrt{2}}{\pi} U_{sLL} \quad \textbf{(3-2)}$$

The line inductance L_L delays the current commutations and it leads to a reduced output voltage. The average value of the dc voltage is then given by [10]:

$$U_d = U_{d0} - \frac{3}{\pi}\omega L_L I_d \quad \textbf{(3-3)}$$

3.1.3 Inverter

The objective in the pulse-width-modulated three-phase inverter is to shape and control the output three-phase voltages in magnitude and frequency. With sinusoidal pulse-width-modulation the line-to-line rms voltage at the fundamental frequency can be written as [10]:

$$U_{LL_1} = \frac{\sqrt{3}}{2\sqrt{2}} m_a U_d \quad \textbf{(3-4)}$$

In the above equation, the inverter is operating in the linear region (amplitude modulation ratio, $m_a \leq 1$), and the DC voltage U_d is assumed to be constant. Further on, the effect of blanking time Δt is ignored. This effect will reduce the output voltage given by Equation (3-4) with the amount ΔV due to Δt. Blanking time is introduced in order to avoid that two switches conduct in one leg at the same time, which causes a short circuit. The change in the output voltage ΔV is proportional to the blanking time and the switching frequency. The selection of semiconductors in the inverter and the used switching frequency will therefore determine the maximum output voltage.

3.2 Drive system requirements

This section presents the calculations made on the suggested motor drive.
According to the specifications, the motor should produce the torque $T_n = 5{,}5\,Nm$ at the rated speed $N_n = 10000\,rpm$. Assuming a motor efficiency of $\eta_{motor} = 0.92$, this gives the electrical power to be fed to the motor:

$$P_{motor} = \frac{T_n \omega_m}{\eta_{motor}} = 6{,}3\ kW \quad \textbf{(3-5)}$$

This power is probably slightly high as the efficiency of the motor is expected to be better.
The losses in the power electronics will increase with the switching frequency. The switching frequency is determined by the fundamental frequency of the output voltage, i.e. the number of poles of the machine and its rotational speed.

To begin with, the efficiency of the rectifier and the inverter are both estimated to 0.96 each. The required power that has to supply the converter is then given by:

$$P_{in} = \frac{P_{motor}}{(\eta_{rectifier} \cdot \eta_{inverter})} = 6{,}8\ kW \quad \textbf{(3-6)}$$

The power factor at which the drive operates from the utility system is essentially independent of the motor power factor [10]. The input ac current drawn by the rectifier contains a large amount of harmonics. The input inductance L_L and the capacitance on the DC side of the rectifier improves the AC current wave form somewhat. The required power factor is assumed to be 0.8, and it is given by:

$$PF = \frac{I_{s1}}{I_s} \cdot \cos(\varphi) = 0{,}8 \quad \textbf{(3-7)}$$

where I_{s1} is the rms line current at the fundamental frequency, and I_s the rms line current. A large amount of harmonics in the line current thus gives a reduced power factor.
In order to obtain a power factor of 0,8 a smoothing line inductance is required. By assuming a constant DC voltage over the capacitor, the smoothing inductance L_s can be determined via the relation between I_d and the line short circuit current I_{sc} [10].

$$PF = 0.8 \Rightarrow \frac{I_d}{I_{sc}} > 0{,}017 \quad \textbf{(3-8)}$$

$$I_{sc} = \frac{U_{sLL}}{\sqrt{3} \cdot 2\pi f \cdot L_s} \quad \textbf{(3-9)}$$

The DC current I_d can be written as:

$$\frac{P_{motor}}{\eta_{inverter}} = U_d I_d \quad \textbf{(3-10)}$$

Equation (3-11) combined with Equation (3-3) gives an expression for I_d:

$$(1.35 \cdot U_{sLL} - \frac{3}{\pi} \omega L_s I_d) \cdot I_d = \frac{P_{motor}}{\eta_{inverter}} \quad \textbf{(3-11)}$$

For a grid line-to-line voltage of 400 V, the relation in Equation (3-8) is fulfilled if $L_s > 1{,}03\ mH$. At this limit, the DC current I_d becomes 12,2 A.
A filter inductance of approximately 1 mH per phase is needed in order to obtain a power factor around 0,8.

The apparent power for dimensioning the drive system can be calculated as:

$$S = \frac{P_{in}}{PF} = \frac{6{,}79 \cdot 10^3}{0{,}8} = 8{,}5\ kVA \quad \textbf{(3-12)}$$

The rms line current I_s can be calculated from the apparent power as:

$$S = \sqrt{3} U_{sLL} I_{s1} = \sqrt{3} U_{sLL} I_s PF \Rightarrow I_s = 15{,}3\ A \quad \textbf{(3-13)}$$

The output voltage is then given by Equation (3-3) combined with Equation (3-4).

$$U_{LL_1} = \frac{\sqrt{3}}{2\sqrt{2}} m_a (U_{d0} - \frac{3}{\pi} \omega L_s I_d) \quad \textbf{(3-14)}$$

With a grid line-to-line voltage of 400 V and a smoothing inductance of 1 mH, the maximum rms output voltage of the fundamental frequency from the inverter becomes:

$$U_{LL_1} = 328V \quad \textbf{(3-15)}$$

This gives the maximum rms phase voltage at the fundamental frequency as:

$$U_1 = \frac{328}{\sqrt{3}} = 189\ V \quad \textbf{(3-16)}$$

This voltage is expected to be a good reference value for use during the machine design process. The above calculations are simplified when neglecting the line impedance. The phase output voltage U_1 used for the machine design process is therefore set equal to 180 V.

4 Thermal modelling

Heat is dissipated in the motor as a consequence of losses. These losses could cause overheating and eventually damage the machine. The slot insulation and the stator windings are exposed to high thermal stresses. Overheating of the permanent magnets might lead to their irreversible demagnetization. Knowledge of the motor's thermal behaviour is thus an important part of the design work. Thermal modelling is a complex task as the temperature distribution in the motor depends on a lot of variables. It requires detailed information on all the machine parts. The result is also strongly influenced by the surrounding temperature and the load conditions of the machine. However, a simplified model can give a rough estimate of the temperature in the different parts of the motor at steady-state operation. This gives helpful information about the critical limits of the machine.
In this chapter, a possible stator frame geometry with coolant ducts is presented. And a simplified thermal model called *The lumped parameter model* is applied to a SMPM machine.

4.1 Design of the stator frame

This section presents a possible design of the stator frame.
According to the specifications, the machine should be cooled with water. The power density of this machine is high due to the small available space. Even with a high efficiency of the machine, the losses are large in relation to the machine volume. Thus, some kind of liquid coolant is required. Water is already in use as coolant for the cutter´s blade. Water is obviously a very good solution. It is suggested that the frame is made by aluminium. This material has good thermal properties as well as a low mass density.

4.1.1 Geometry of the frame

The aluminium frame is used to transport the heat to the coolant. The heat transfer capacity of the frame depends on its geometry. If the stator frame is made in aluminium with spiral shaped cooling channels, the temperature difference along the stator frame surface can be kept small [11]. A suggested geometry is shown in Figure 4-1.

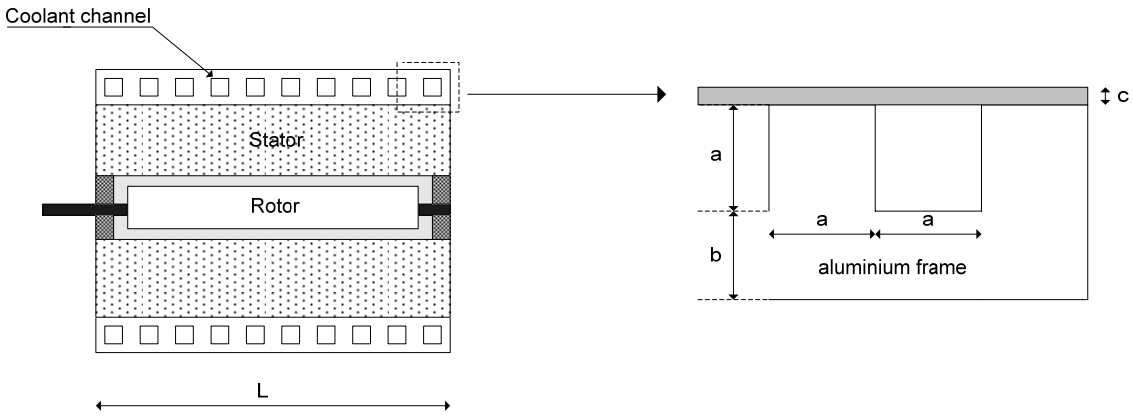

Figure 4-1: Suggested frame geometry

The dimension of the geometrical parameter *a* in Figure 4-1 determines the duct cross-sectional area. This parameter is strongly influenced by the amount of losses that are supposed to be transported with the water together with the coolant flow. This is studied further in section 4.1.2. The parameter *c* is suggested to be kept as small as possible in order to gain some space, approximately 1 mm. In order to smooth out the axial temperature differences along the inner frame surface it is probably a good idea to choose parameter *b* in a similar range as *a*. But active space for the machine is given a higher priority, *b* is suggested to be 2 mm if possible. This will limit the amount of mechanical stress that the stator frame can withstand. **Therefore it is important that the mounting of the machine onto the cutter chassis is not made via the stator frame.**

4.1.2 Required coolant flow

In order to transport all the losses away from the machine, the flow of the coolant has to exceed a minimum limit. This flow limit is depending on the specific heat capacity of the coolant and the allowed temperature increase of the coolant between entering the channel to coming out. In order to avoid a large temperature difference in the axial direction of the machine it is suggested to keep the temperature increase of the coolant as low as possible, a reasonable temperature increase is
5^{o} C. For a given amount of losses P_{loss}, the required minimum flow can be calculated as follows:

$$Q_{\min} = \frac{P_{loss}}{\rho_c C_{p_c} \Delta T} \qquad \textbf{(4-1)}$$

where ρ_c and C_{p_c} are the mass density and the specific heat capacity of the coolant respectively. ΔT is the temperature increase of the coolant. One can see that a small ΔT gives a large flow. In order to reach that flow, the cross-sectional area of the coolant channel can not be too small, as that would require an unreasonable high pressure in the duct.

Assuming a motor efficiency of 92 % and a coolant temperature increase of 5^{o} C, the required flow becomes approximately 1,5 litre/min according to Equation (4-1). The water speed is given by:

$$v_{\min} = \frac{Q_{\min}}{a^2} \qquad \textbf{(4-2)}$$

A suggested cross sectional area of the coolant ducts is approximately 50 mm^2. If parameter *a* in figure 4-1 is set to 7 mm the required water speed becomes approximately 0,5 m/s. This seems to be a reasonable speed.

4.2 Thermal modelling of the machine

In this section the electric equivalent circuit used for the thermal modelling of the machine is described. The representation of the different machine parts in the circuit is discussed. The method used to calculate the steady-state temperatures in the machine is also presented.

4.2.1 The lumped parameter model

Thermal networks are used frequently for modelling different kinds of system. In general, the geometrical complexity of an electrical machine requires a large thermal network in order to get an accurate solution. However, the geometrical symmetries of the machine can be used to reduce the order of the model. In [11], a thermal model of a water cooled permanent magnet motor is presented. Since the machine modelled in [11] is quite similar to the machine treated in this project, that thermal model is used as a start point. The distributed thermal properties have been lumped together to form a small thermal network representing the entire machine. A network with eight nodes is used to model the machine, each node representing a specific part or region of the machine (see Figure 4-2). The thermal resistances between the nodes include conductive and convective heat transfer. They depend on geometry and material properties. If the heat generation (losses) is known in each node, the correspondingly temperature rise relative to a reference temperature can be calculated.

4.2.2 Choice of the nodes in the lumped parameter model

Nodes should be present to the lumped parameter models where losses have to be introduced at that point, where the temperature at a specific point is important and where there is a change of material at that point.

The cooling medium is represented with one node. The heat transfer between the machine and the cooling medium is modelled by assuming a constant average temperature of the coolant. The solution of the equation system gives therefore the temperature rises in the machine parts with reference to the coolant temperature. The aluminium frame is represented with one node. Two nodes are used to model the stator core, one placed in the yoke and one in the teeth. The stator winding is represented by two nodes, one for the coil side, and one for the End-winding where the highest temperature of the machine is expected.
Predicting the temperature of the permanent magnets is of great importance. Overheating of the permanent magnets can cause permanent demagnetization, and consequently permanent damage to the machine. Therefore one node is assigned to the permanent magnets.
In addition one node is later assigned to the rotor surface giving the possibility to add frictional losses on the surface. Bearing temperature is an important aspect when the lifetime of an electrical machine is estimated. This temperature is depending of the rotor losses, the load and the operational speed. The rotor losses are expected to be quite low but since the machine is operating at a relative high speed one node is assigned to the bearings.

4.2.3 Electric equivalent circuit

This section present the electric equivalent circuit used for the thermal modelling of the machine. The equations for the thermal resistances in the following two circuits can be found in Appendix A. The thermal network suggested in [11] was used as a start, Figure 4-2.

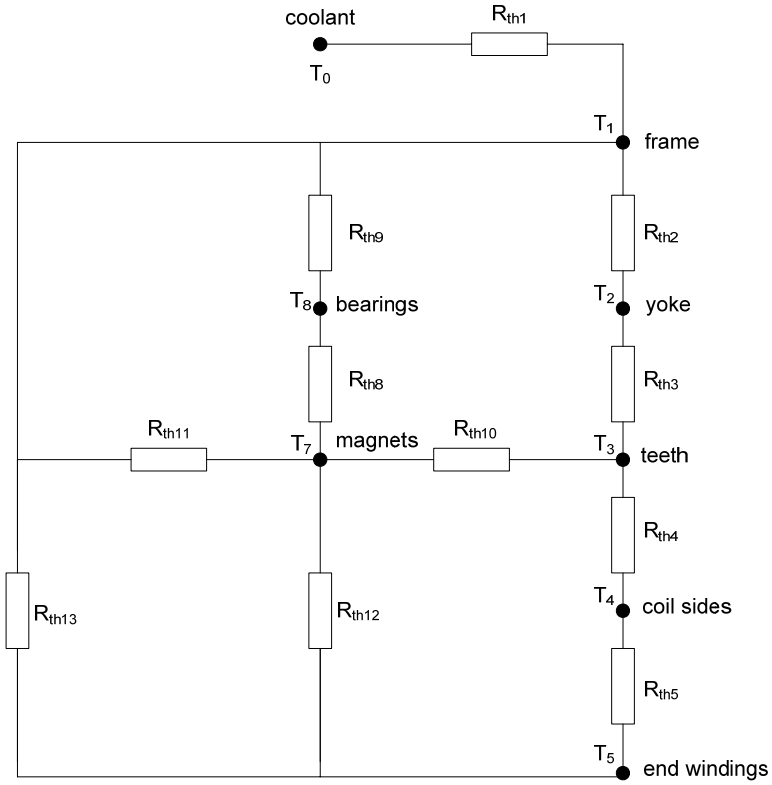

Figure 4-2: First electric equivalent circuit [11]

Losses were calculated and estimated in order to assign a specific loss component to each node. The sensitivity of the system was studied and resulted in a simplified model. The thermal resistances via the internal air between frame, End-winding and magnets ($R_{th11}, R_{th12}, R_{th13}$) were not affecting the result marginally. Since they were complex to calculate and several uncertain parameters were found these resistances were treated as large. This resulted in the simplified model shown in Figure 4-3. The injected losses are inserted as equivalent current generators. In addition to the previous model, one node has been assigned to the rotor surface giving the possibility to add frictional losses.

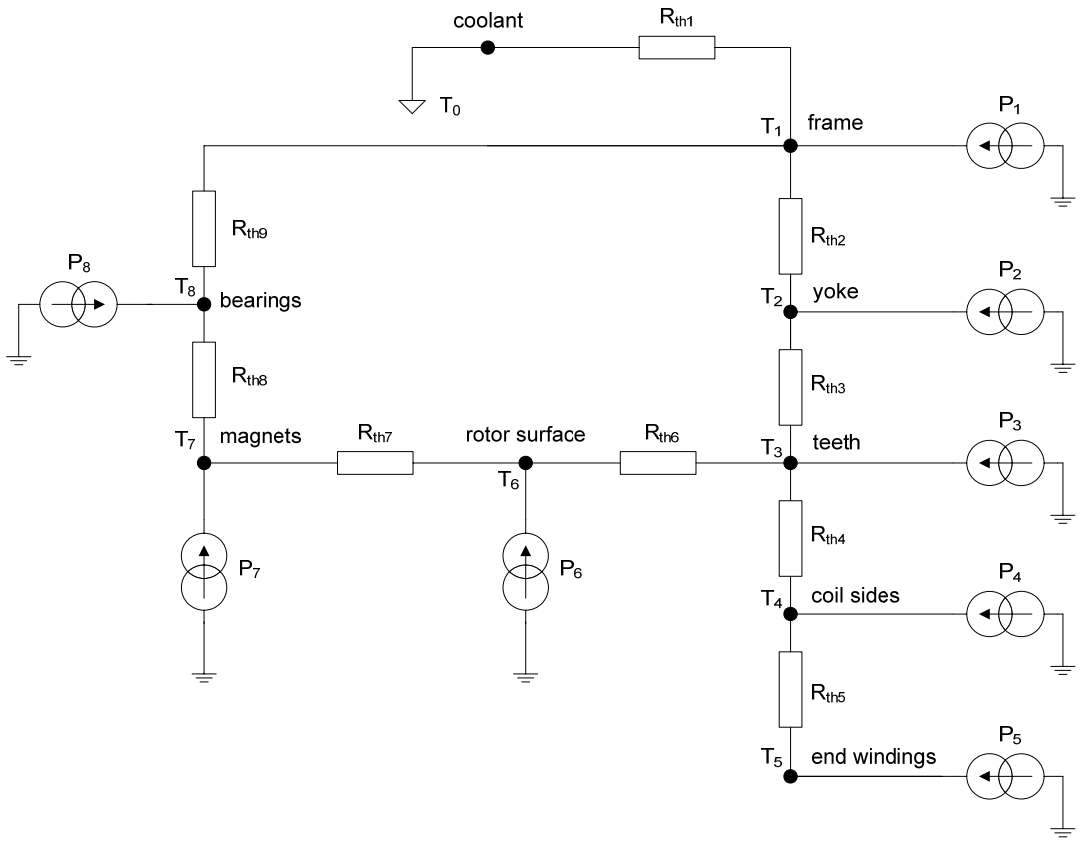

Figure 4-3: Electric equivalent used during the design process

This circuit is used during the design process in order to predict the different temperatures in the machine.

4.2.4 Thermal modelling of the machine parts

The thermal resistances in the model are calculated from the equivalent conduction and convection resistances of the different parts of the motor. Their expressions can be found in Appendix A. This section describes the uncertainties that have appeared during these calculations.

The length of the machine is limited to 80 mm according to the specifications. It is assumed that this length should include the bearings. The maximum active length *L* is therefore set to 55 mm and equal to the stator core length, l_{Fe}. The useful iron length, l_{use} is given by:

$$l_{use} = k_{Fe} l_{Fe} \tag{4-3}$$

where k_{Fe} is the stacking factor due to the insulation between the iron sheets. This factor is depending on the thickness of the iron sheets. k_{Fe} is assumed to be 0,95.
The average conductor length of half a turn of the winding coil is given by [11]:

$$l_{av} = l_{Fe} + 1.2\tau_p + l' \tag{4-3}$$

where τ_p is the pole pitch and the quantity l' is equal to 50 mm, which is valid for small machines [11]. l' seems to be quite large in relation to this machine and was therefore set to 40 mm instead.

The thermal resistance between the coil sides and the stator teeth greatly affects the temperatures in the machine. The accuracy of the result depends on the modelling of this resistance. The radial thermal conductivity of the winding is approximated with an equivalent conductivity due to the fill factor.

$$k_{winding} = k_{cu} f_s + k_{ins}(1 - f_s) \tag{4-4}$$

where k_{cu} and k_{ins} are the thermal conductivities of the copper and the insulation, respectively. f_s is the slot fill factor. This equivalent conductivity is used when modelling the stator winding. Further on, the contact resistance between the coil and the stator teeth is modelled with an air layer d_{air} and an insulation layer d_{ins}, the thickness of these layers were assumed to be 0,1 mm each. Lindström refer to an experimental investigation on a 15 kW IM that resulted in an equivalent air layer thickness of 0,3 mm [11]. Notice that the machine treated in this thesis is much smaller. These values of course depend a lot on the manufacturing process but can easily be changed in order to develop the model further.

The contact resistance between the aluminium frame and the stator iron lamination is modelled with an equivalent air layer g_e that is assumed to be 30 µm thick. This corresponds to a contact pressure of approximately $3 \cdot 10^6 \, N/m^2$ [12]. For simplicity the same contact resistance is used to model the resistance between the shaft and the rotor iron lamination.

4.2.5 Steady state analysis

A thermal network with n+1 nodes is represented by n coupled algebraic equations. The temperature rise at the nodes relative to a reference temperature are calculated from:

$$T = G^{-1} P \tag{4-5}$$

Where P is the loss vector containing the losses assigned to each node.

$$P = \begin{bmatrix} P_1 \\ P_2 \\ \vdots \\ P_n \end{bmatrix} \tag{4-6}$$

G is the thermal conductance matrix, defined as:

$$G = \begin{bmatrix} \sum_{i=1}^{n} \frac{1}{R_{1,i}} & -\frac{1}{R_{1,2}} & \cdots & -\frac{1}{R_{1,n}} \\ -\frac{1}{R_{2,1}} & \sum_{i=1}^{n} \frac{1}{R_{2,i}} & \cdots & -\frac{1}{R_{2,n}} \\ \vdots & \vdots & \ddots & \\ -\frac{1}{R_{n,1}} & -\frac{1}{R_{n,2}} & \cdots & \sum_{i=1}^{n} \frac{1}{R_{n,i}} \end{bmatrix} \tag{4-7}$$

$R_{i,j}$ is the thermal resistance between node i and node j.

Results given by this thermal model are presented in chapter 6.

5 Loss models

In this chapter, all the loss models that are taken into account during the machine design process are defined. The models are based on the theory presented in section 2.4.

5.1 Copper loss model

The copper losses are calculated according to Equation (2-10) and Equation (2-11) presented in chapter 2. However, the copper resistance is temperature dependent through the copper resistivity. This is taken into account by introducing the following expression for the copper resistivity [3]:

$$\rho_{cu} = 2 \cdot 10^{-8} (1 + 0{,}004 (T - 25)) \tag{5-1}$$

where T is the temperature of the winding. The temperature of the winding can not be calculated without knowing the copper losses. As a worst case approach, T is set equal to the maximum allowable winding temperature 120^{o} C.
In the thermal model the winding is represented by two nodes, the End-windings and the coil sides. The ratio between the coil side length and the average length of half a winding turn is used to estimate the losses in each node. Thus, for the coil sides the copper losses are given by:

$$P_{cu\_cs} = \frac{l_{Fe}}{l_{av}} P_{cu} \tag{5-2}$$

and the losses in the End-windings are given by:

$$P_{cu\_ew} = \left(1 - \frac{l_{Fe}}{l_{av}}\right) P_{cu} \tag{5-3}$$

5.2 Iron loss models

During the design process the iron losses in the stator core are calculated analytical while the rotor iron losses are neglected. A time stepped time stepped finite element method is used in order to verify the results. This simulation gives an estimation of the rotor iron losses as well.
The chosen iron lamination is M400-50A manufactured by Cogent Power Ltd at Surahammars Bruks AB in Sweden. A thin lamination may give less iron losses then a thick lamination. The investigated material has a thickness of 0,5 mm. The material was chosen for two main reasons. This material is available in the material database in Flux2D which is the software used for verification of the analytical model, and data from the manufacturer was available in a suitable range of frequencies. It is as well a middle range quality of lamination.

5.2.1 Analytical model

The iron losses in the stator core are calculated using the modified loss model valid for non sinusoidal flux densities described in 2.4.2. But determination of the hysteresis and the eddy current loss constants in Equation (2-12) is necessary. This is made by curve fitting from manufacturer data.

For a four pole machine, the electrical frequency in the stator winding is 333 Hz at 10 000 rpm. Iron loss data was not available for this frequency so data for the frequencies 200 and 400 Hz were used instead. This data corresponds to a sinusoidal flux density varying from 0 to 1,5 Tesla. The loss coefficients k_h and k_e are chosen in such a way that they minimize the relative error of the loss density obtained by Equation (2-12).

$$\min \sum_{f} \sum_{\hat{B}} \frac{p_{iron}(f,\hat{B}) - p_{data}(f,\hat{B})}{p_{data}(f,\hat{B})},\ f = 200;400\ Hz,\ \hat{B} = 0;0{,}1;0{,}2.....1{,}5\ T \qquad \textbf{(5-4)}$$

Equation (5-4) is minimized for $k_h = 34{,}12 \frac{\mathrm{Ws}}{\mathrm{T}^2 m^3}$ and $\mathrm{k_e} = 0{,}028 \frac{\mathrm{Ws}^2}{\mathrm{T}^2 \mathrm{m}^3}$, with the Steinmetz constant β_{St} set to 2,0. It is the fixed value used as default in Flux2D. The results at the two frequencies for these values are shown in Figure 5-1 and Figure 5-2. Note that the losses in the figures are given in W/kg instead of W/m^3, which differ by the iron lamination mass density of 7700 kg/ m^3.

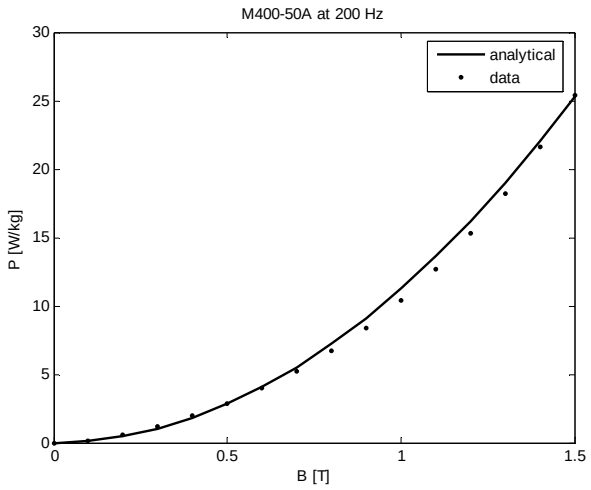

Figure 5-1
Losses at sinusoidal flux density of 200 Hz

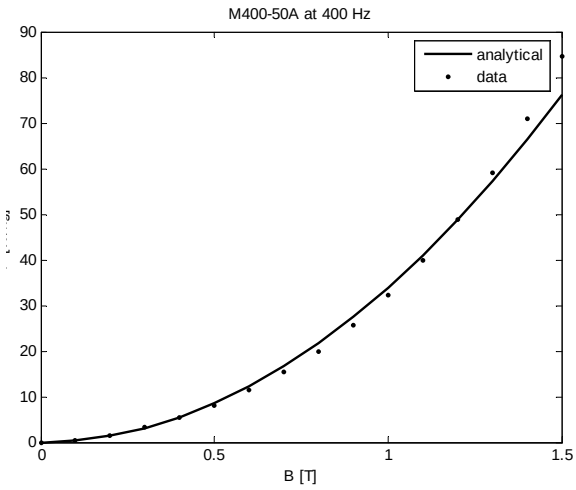

Figure 5-2
Losses at sinusoidal flux density of 400 Hz

These loss coefficients are used when calculating the iron losses in the stator core analytically.

5.2.2 Finite element model

Flux2D is the FEM software used for verification of the analytical results. In the post processing options, Flux2D can calculate the iron loss in each region with the following equation [3]:

$$p_{iron\_FEM} = k_{hyst}\hat{B}^2 k_f f + \frac{1}{T}\int_0^T \left(\frac{\sigma_{iron} d_{lam}^2}{12}\left(\frac{dB(t)}{dt}\right)^2 + k_{exc}\left(\frac{dB(t)}{dt}\right)^{\frac{3}{2}} \right) k_f dt \qquad \textbf{(5-5)}$$

where d_{lam} is the iron lamination thickness and σ_{iron} is the conductivity of the iron lamination, $\sigma_{iron} = 2{,}38 \cdot 10^6\,(\Omega m)^{-1}$. This equation includes the hysteresis losses, the eddy current losses and the excess losses. Note that the hysteresis loss coefficient k_{hyst} and the excess loss coefficient k_{exc} are not the same as the loss coefficients in Equation (2-12).

In a simplified case, assuming that the variation of the flux density is sinusoidal, the loss density becomes [13]:

$$p_{iron\_FEM'} = k_{hyst}\hat{B}^2 f + \pi^2 \frac{\sigma_{iron} d_{lam}^2}{6}(\hat{B} f)^2 + 8{,}67\, k_{exc}(\hat{B} f)^{\frac{3}{2}} \qquad \textbf{(5-6)}$$

with k_{hyst} given in $\frac{Ws}{T^2 m^3}$ and k_{exc} given in $\frac{W}{m^3}\left(\frac{s}{T}\right)^{\frac{3}{2}}$.

However, the values of these coefficients had to be calculated to be introduced in the FEM software. Once again a curve fit based on the available loss data is made. In order to obtain reliable result on the iron losses in the machine (rotor loss + stator loss), the loss coefficients have to be valid for a wide frequency range. Because of the high frequency of the harmonics that contribute to the rotor losses. When the rotor is synchronized, the fundamental of the flux does not create any losses in the rotor.
The rotor losses are partly due to the harmonic content in the airgap flux and partly due to the varying reluctance in the airgap that distorts the main flux in the rotor core.
The 5th and 7th space harmonics cause a variation of the flux density in the rotor at a frequency equal to six times the fundamental, this is approximately 2000 Hz. The influence of the third harmonic is expected to be of minor importance due to the choice of the pole angle. This is described further in chapter 6. Optimum values of k_{hyst} and k_{exc} for the frequency range 200, 2500 Hz are obtained by minimizing the following expression:

$$\min \sum_f \sum_{\hat{B}} \frac{p_{iron\_FEM'}(f,\hat{B}) - p_{data}(f,\hat{B})}{p_{data}(f,\hat{B})} \qquad \textbf{(5-7)}$$

for f = 0,2; 0,4; 1,0; 2,5 kHz and $\hat{B}$ = 0; 0,1; 0,2…..1,5 T.

This resulted in a negative value of the excess loss coefficient. This has no meaning physically and is obtained because of the analytical expression used for the iron loss calculation. In Equation (5-3) used by Flux2D, the Steinmetz constant is equal to 2. This is a default value and cannot be changed. The actual value of the Steinmetz constant for the

selected material is probably slightly lower. This resulted in a too large hysteresis loss which was compensated by the negative excess loss in order to minimize the relative error.

In order to bypass this problem, the frequency range is decreased and adapted for the stator frequency. For the stator core losses, the coefficients were $k_{hyst} = 167{,}17$ and $k_{exc} = 0{,}439$ (Equation (5-7) with f = 200, 400 Hz). These loss coefficients have been used in the time stepped solving process when determining the stator core losses only.

In a similar way a new set of loss coefficients are determined for use in the rotor loss calculation. The optimization of Equation (5-7) is performed with data corresponding to the frequencies 1,0 and 2,5 kHz with the excess loss coefficient set to zero.

An optimal solution is found for $k_{hyst} = 14{,}72 \frac{Ws}{T^2 m^3}$.

Figure 5-3 and Figure 5-4 show a comparison with the loss data. Note that the losses are given in W/kg.

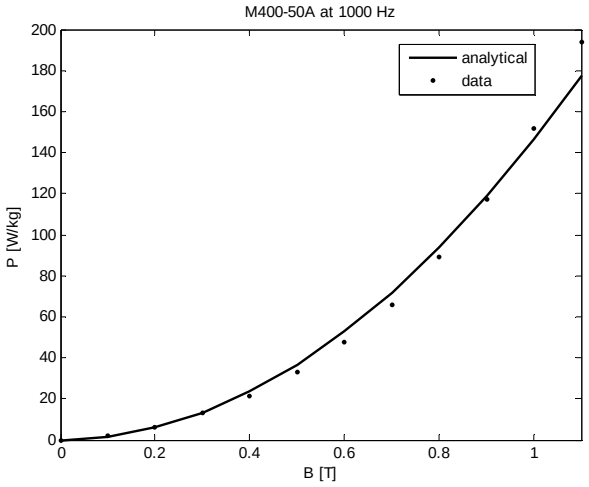

Figure 5-3
Model for the rotor losses at 1000 Hz

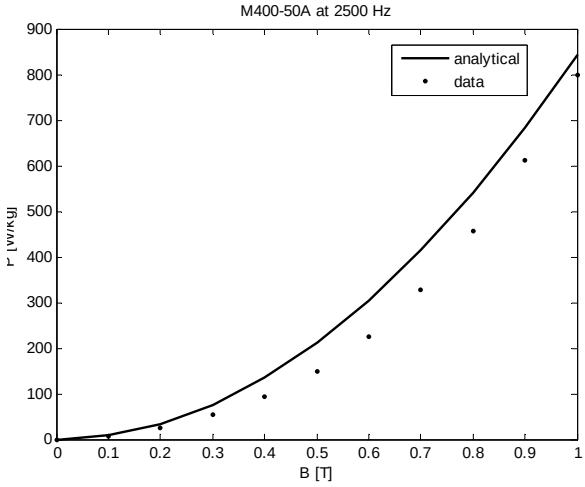

Figure 5-4
Model for the rotor losses at 2500 Hz

5.3 Magnet loss model

There are also losses in the magnets due to eddy currents. They are probably very small but they are however estimated and included in the thermal model. The magnet losses are assumed to be proportional to the magnet area exposed in the airgap. The loss per square millimetre is assumed to be 2 mW/mm^2. This results in a total loss due to eddy currents in the magnets in the range 6-10 W.

5.4 Mechanical loss models

Bearing losses and windage losses may not have a big influence of the total losses in this specific machine. But as they have been theoretically studied the models are applied anyway.

5.4.1 Bearing loss model

The mechanical dimensioning of the machine was quite unknown. But after a discussion with project manager Daniel Ericson at Electrolux AB, some assumptions could be made.
A reasonable shaft diameter is 12 mm. And as the power is transferred through a belt drive the axial thrusts on the bearings are neglected. The radial force on the output shaft bearing can be assumed to be approximately 400 N. The force on the second bearing is probably lower, but as a worst case approach, it is assumed to be the same as for the output shaft bearing.
An estimation of the losses in the bearings can be made using Equation (2-29). The coefficient of friction is assumed to be 0,0015 [7]. The total losses for the two bearings become:

$$P_{f_b} = 2\left(\frac{1}{2}\mu_f F_b d_i\right)\omega_m \approx 8W \qquad \textbf{(5-8)}$$

On the SKF website, it is possible to calculate an accurate value of the total power loss in a specific bearing. The required parameters are the rotational speed, viscosity of the lubricant and the forces acting on the bearing. A suggested bearing type is SKF 6201.
A calculation was made for that bearing using the SKF website. The viscosity of the lubricant was set to 8,25 mm^2/s, which SKF recommends at an operating temperature of 50° C and a rotational speed of 10000 rpm. The result was an increased power loss of approximately 60 % compared with the result in Equation (5-8). The web calculation was made with different radial bearing loads at nominal speed. With these results, an equation for the total bearing losses could be developed. The expression is similar to Equation (2-30) with one load dependent part and one load independent part. The total bearing losses are approximated with the following equation:

$$P_{f_b} = \left(T_0 + k_b F_b\right)\omega_m \qquad \textbf{(5-9)}$$

Figure 5-5 shows the almost linear relation between the power losses and the bearing load for a constant rotor speed at 10000 rpm. With suitable values of k_b and T_0 the approximation gives reliable results in the given interval. This approximation could be useful when the bearing load is uncertain.

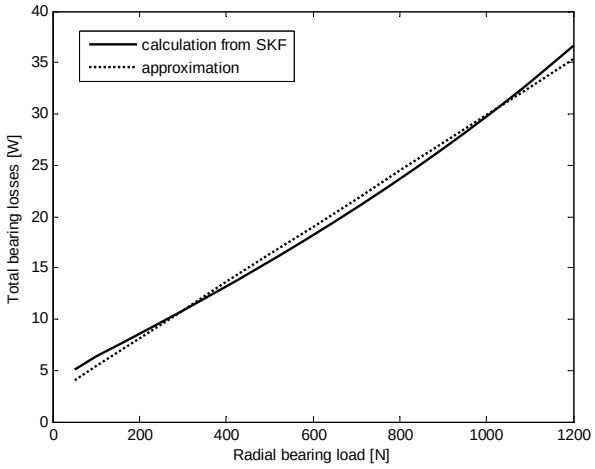

Figure 5-5 Bearing loss model

Based on these results, the total bearing losses can be assumed to be approximately 14 W at a radial bearing load of 400 N. This value is important when determining the bearing temperature as well as when estimating the bearing lifetime.

5.4.2 Windage loss model

The rotor loss due to air friction is calculated according to the previous theory, i.e. as for an enclosed rotating cylinder neglecting the effect of the rotor end surfaces. The roughness coefficient k_f in Equation (2-26) is given the value 1,25 based on Saari:s measurements in [5], even though it is related to a much higher peripheral speed. The result is not expected to be strongly influenced by this factor when the actual peripheral speed is quite low.
The windage losses were studied as a function of the rotor diameter at a rotational speed of 10000 rpm and an active machine length of 55 mm.

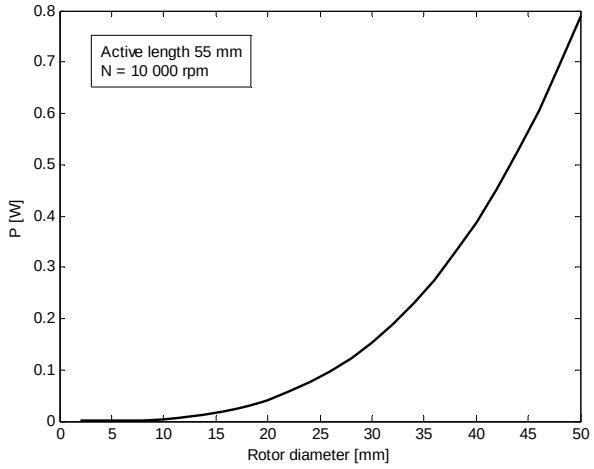

Figure 5-6 Windage losses as a function of the rotor diameter

As this result shows, the total loss on the rotor surface is negligible for this specific design. The reason for the low frictional loss is the peripheral rotor speed, i.e. the small rotor diameter. But it may have an influence on other designs, especially for larger or faster machines.

6 Analytical design of the SMPM motor

Matlab is the software used during the analytical design process. The main design program was developed by Florence Libert during her licentiate thesis [3]. The main equations used in this program are presented in section 6.1. An optimization program was also included. The different loss models described in this thesis have been developed and implemented into the main program. The thermal model and the bandage calculations are also included.

The main program is used to study the performance of specific machine geometries. The optimization program can be used with different objective functions. The output data from the optimization is a machine geometry. The optimization procedure is described with the flow-chart given in Appendix B. These programs are used during the parameter study in section 6.2. The parameter study led to a suggested machine design presented in section 6.3.

6.1 Design process

In this section, the requirements and the constraints that the design relies on are summarized. The geometrical parameters are defined and the main equations used during the magnetic and the electric design processes are presented.

6.1.1 Constraints and requirements

To start the design process, the constraints and the requirements of operation have to be defined.

At rated operation the requirements are:

- a speed of 10 000 rpm
- an axis torque of 5,5 Nm

The constraints of the dimensions are:

- outer diameter ≤ 90 mm (the suggested stator frame in 4.1.1 not included)
- active length ≤ 55 mm (according to the assumptions made in 4.2.4)
- shaft diameter = 12 mm (according to the assumptions made in 5.3.1)

The maximum inverter output phase voltage U_1 is limited to approximately 180 V according to section 3.2. Further on, the current density in the conductors is limited to 10 A/mm^2 (the constraint was inherited from the stage where the thermal model was implemented).

Constraints regarding the flux density [3]:

- fundamental airgap flux density $\hat{B}_{\delta} \approx 0{,}9$ T
- maximum flux density in the stator yoke $\hat{B}_{sy} \approx 1{,}4$ T
- maximum flux density in the stator teeth $\hat{B}_{st} \approx 1{,}6$ T
- maximum flux density in rotor yoke $\hat{B}_{ry} \approx 1{,}4$ T

The magnet characteristics are assumed as follows [3]:

- remanence flux density $B_r = 1{,}08$ T (at a temperature of 60^{o} C)
- demagnitisation flux density $B_d = -0{,}2$ T
- relative permeability $\mu_r = 1{,}03$

Due to the relatively small machine, a large number of poles are probably not suitable. That would decrease the available space for the winding too much, even if the number of slots per pole and phase is low. When the speed of the machine is high, a large number of poles would require a very high fundamental frequency of the stator current. This would increase the iron losses as well as the switching losses. If the pole angle is set equal to 120 electrical degrees the third space harmonic is suppressed.

The machine design possibilities are therefore reduced to:

- number of poles $p = 4$
- number of slots per pole and phase $q = 1$
- half pole angle $\alpha = 60$ electrical degrees

A high stator slot fill factor improves the machine performance a lot. But a high fill factor makes the manufacturing process more difficult. The stator slot fill factor f_s is assumed to be 0,5. This is a reasonable value that should be possible to obtain in practice.

6.1.2 Geometrical properties

In this section, the geometrical parameters of the SMPM machine are defined.
The parameters that should be determined are illustrated in Figure 6-1 and Figure 6-2.

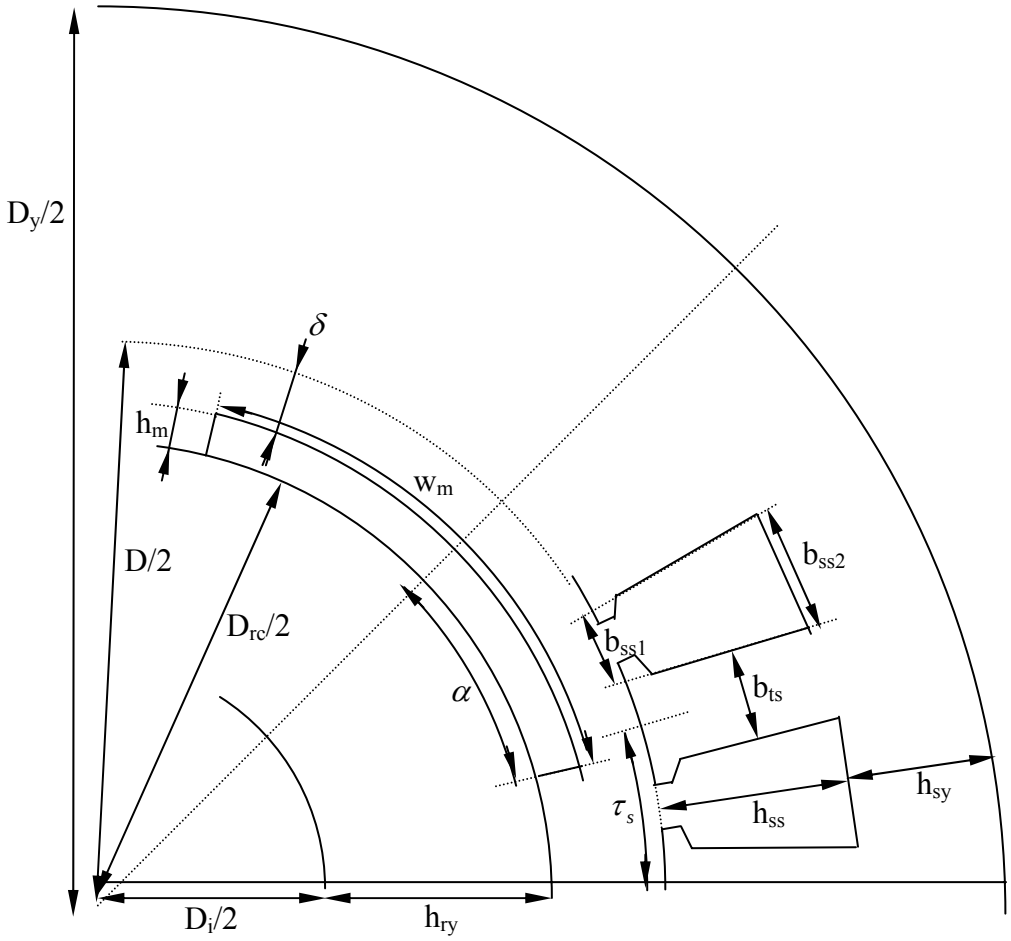

Figure 6-1 Cross section of a 4-pole SMPM with dimensions [13]

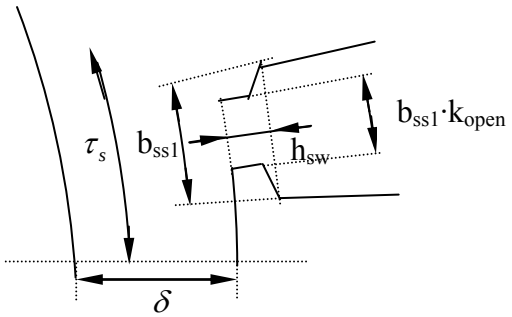

Figure 6-2 Illustration of the dimensions in the area of the stator slot opening [13]

6.1.3 Magnetic properties

A good estimation of the fundamental airgap flux density is important when the design procedure relies on it. To start with, the airgap flux density is assumed to have a rectangular shape as wide as the magnets with a maximum value B_m given by:

$$B_m = \frac{B_r k_{leak}}{1 + \frac{\mu_r \delta k_C}{h_m}} \tag{6-1}$$

Where μ_r is the relative magnet permeability and k_C the Carter factor [3].

$$k_C = \frac{\tau_s}{\tau_s - \frac{(k_{open} b_{ss1})^2}{b_{ss1} k_{open} + 5\delta}} \tag{6-2}$$

The factor k_{leak} takes the magnetic leakage between the magnets into account. Flux2D simulations are used in order to determine this factor. More information regarding the leakage factor can be found in [3]. The magnitude of the fundamental airgap flux density is then calculated as follows:

$$\hat{B}_\delta = \frac{4}{\pi} B_m \sin(\alpha) \tag{6-3}$$

where α is half the pole angle in electrical degrees. As described in [3], the analytical model is improved further taking the influence of the stator slot opening into account. The area within the stator slot opening creates locally increased airgap reluctance. Thus the airgap flux density is reduced under the stator slot opening. Taking this into account gives a more accurate analytical value of the fundamental airgap flux density. This model is studied further in chapter 7.

In addition to the flux created by the magnets the armature current creates a flux. This is referred to as armature reaction. The armature reaction distorts the airgap flux created by the magnets. The armature reaction for machines with a large airgap such as SMPM machines is relatively small. Assuming the stator current produces a sinusoidal flux density, its peak value $\hat{B}_{\delta,arm}$ in the airgap is [13]:

$$\hat{B}_{\delta,arm} = \frac{3\mu_0}{\pi\left(\delta k_C + \frac{h_m}{\mu_r}\right)} q\, n_s\, k_{w1}\, \hat{I}_1 \tag{6-4}$$

In the airgap, the fundamental of the armature flux density is phase shifted by the angle β relative to the fundamental magnet flux density. $\beta = 90^{\,o}$ usually to optimize the ratio $\frac{T}{\hat{I}_1}$.

The maximum flux density in the stator teeth is then calculated as [3]:

$$\hat{B}_{st} = \frac{B_m 2\alpha(D-2\delta)}{pb_{ts}\left(\frac{q_s}{p}-q\right)k_{Fe}} \quad \textbf{(6-5)}$$

It can be noted that only the flux created by the magnets is taken into account.
Where q_s is total number of stator slots and k_{fe} is the iron stacking factor. The leakage flux flowing through the tooth shoe only is neglected.

The maximum flux density in the rotor yoke is given by [3]:

$$\hat{B}_{ry} = \frac{\alpha B_m (D-2\delta)}{pk_{Fe}h_{ry}} \quad \textbf{(6-6)}$$

The maximum flux density in the stator yoke is calculated as follows [3]:

$$\hat{B}_{sy} = \left(\frac{B_m 2\alpha(D-2\delta)L}{p} + \frac{6\mu_0 q n_s \hat{I}_1 k_w \sin\left(\frac{\pi}{2}-\alpha\right)DL}{p\pi\left(\delta k_C + \frac{h_m}{\mu_r}\right)} \right) \frac{1}{2Lk_{Fe}h_{sy}} \quad \textbf{(6-7)}$$

where n_s is the number of conductors per slot, $\hat{I}$ is magnitude of the conductor current, k_w is the winding factor and μ_r is the relative permeability of the magnets.

In order to avoid demagnetisation of the magnets, no part of the magnets should be exposed to a flux density lower than B_d. This sets the following limit on the flux density produced by the stator current:

$$\hat{B}_{\delta,arm} \leq B_m - B_d \quad \textbf{(6-8)}$$

This equation gives the maximum allowable stator current calculated in section 6.1.4.

6.1.4 Electrical properties

The required stator current loading is calculated from the rated torque T_n as:

$$\hat{S}_1 = \frac{4T_n}{\pi L \hat{B}_\delta k_{w1}(D-\delta)^2 \sin(\beta)} \quad \textbf{(6-9)}$$

where L is the active length of the machine and k_{w1} is the winding factor for the first harmonic. For non salient machines, maximum torque is achieved if β = 90°, i.e. only q-axis current. The winding factor for the first harmonic can be written as [13]:

$$k_{w1} = \frac{\sin\left(\frac{\pi}{6}\right)}{q\sin\left(\frac{\pi}{6q}\right)} \quad \textbf{(6-10)}$$

The required peak value of the total stator current per slot is determined via the stator current loading as follows:

$$n_s \hat{I}_1 = \hat{S}_1 \tau_s \tag{6-11}$$

where n_s is the number of conductors per slot.

The current density in the conductors *J* is calculated via the copper area per slot. But first the stator slot area is calculated as:

$$A_{sl} = \frac{b_{ss1} + b_{ss2}}{2}(h_{ss} - h_{sw}) \tag{6-12}$$

which gives the copper area per slot as:

$$A_{cu} = f_s A_{sl} \tag{6-13}$$

where f_s is the stator slot fill factor. The maximum current density is then given by:

$$\hat{J} = \frac{n_s \hat{I}_1}{A_{cu}} \tag{6-14}$$

According to Faraday´s law, the magnet flux linkage $\Psi_m(t)$ will induce a voltage *E* in each phase winding. The induced phase voltage *E* is given by:

$$E = \frac{d\,\Psi_m(t)}{dt} = N_s \frac{d\,\Phi_m(t)}{dt} \tag{6-15}$$

where N_s is the equivalent number of turns per phase and $\Phi_m(t)$ is the fundamental magnet flux linked to one turn of the coil.

$$N_s = \frac{p}{2} q\, n_s k_{w1} \tag{6-16}$$

$$\Phi_m(t) = \frac{2\hat{B}_\delta L (D-\delta)}{p}\sin(\omega_e t) \tag{6-17}$$

The peak value of the fundamental induced voltage *E* can now be determined as:

$$\hat{E} = N_s \max\left(\frac{d\Phi_m(t)}{dt}\right) = \hat{B}_\delta L (D-\delta)\,\omega_e\, q\, n_s\, k_{w1} \tag{6-18}$$

For a non salient synchronous machine, the d- and q-axis synchronous inductances are equal, this inductance can be written as:

$$L_d = L_q = L_l + L_m \tag{6-19}$$

where L_l is the leakage inductance and L_m is the magnetizing inductance. These inductances are calculated as follows [13]:

$$L_l = p\, q\, n_s^2\, L\, \mu_0\, \lambda_1 \tag{6-20}$$

$$L_m = \frac{3}{\pi}(q\, n_s\, k_{w1})^2 \frac{\mu_0}{\delta\, k_C + \frac{l_m}{\mu_r}}(D-\delta)\, L \qquad \textbf{(6-21)}$$

where λ_1 is a coefficient depending on the slot geometry, details can be found in [13]. Note that the end-winding inductance not is included in Equation (6-20) and Equation (6-21).

A phasor diagram that shows the couplings between the different electrical properties is shown in Figure 6-3.

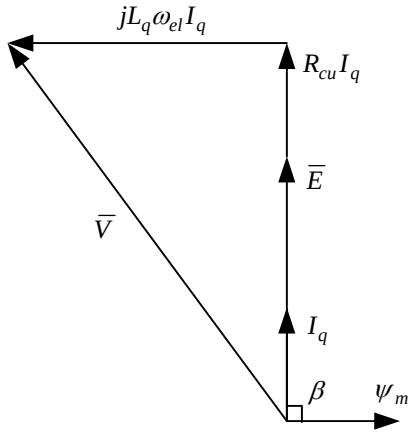

Figure 6-3 The SMPM machine at rated motor operation

The number of conductors per slot n_s is determined from the equation for the external voltage V (the inverter output voltage). When $I_q = I_1$, the phasor diagram gives:

$$\hat{V}^2 = (\hat{E} + R_{cu}\, \hat{I}_1)^2 + (L_q\, \omega_{el}\, \hat{I}_1)^2 \qquad \textbf{(6-22)}$$

The dependency of the number of conductors per slot in Equation (6-22) is not obvious. This is clarified by rewriting the inductance, the resistance and the induced voltage as:

$$\begin{aligned} L_q &= n_s^2 L_q' \\ R_{cu} &= n_s^2 R_{cu}' \\ E &= n_s E' \end{aligned} \qquad \textbf{(6-23)}$$

Combining Equation (6-22) and Equation (6-23) gives:

$$\hat{V}^2 = n_s^2(\hat{E}' + R_{cu}'\, n_s \hat{I}_1)^2 + n_s^2(L_q'\, \omega_{el}\, n_s \hat{I}_1)^2 \qquad \textbf{(6-24)}$$

The ampere turns $n_s\, \hat{I}_1$ are known according to Equation (6-11), thus the number of conductors per slot can be determined as:

$$n_s = \frac{\hat{V}}{\sqrt{(\hat{E}' + R_{cu}'\, n_s \hat{I}_1)^2 + (L_q'\, \omega_{el}\, n_s \hat{I}_1)^2}} \qquad \textbf{(6-25)}$$

Note that $\hat{V} = \sqrt{2}\,U_1$. The peak value of the stator current is then given as:

$$\hat{I}_1 = \frac{\left(n_s\ \hat{I}_1\right)}{n_s} \tag{6-26}$$

The maximum stator current that is allowed in order to avoid demagnetisation of the magnets is given by [13]:

$$\hat{I}_{\max} \le \pi \frac{B_r\ h_m - B_d\,(h_m + \mu_r\ \delta\, k_C)}{3\,\mu_0\ \mu_r\ q\, n_s\ k_{w1}} \tag{6-27}$$

6.2 Parameter study

In this section, the influence of different parameters on the motor performance is studied.
To start with, the stator geometry is kept constant while the airgap and the magnet thicknesses are varied. Theses two parameters are then kept constant while the influence of the rotor diameter and the stator geometry is studied. The studied machine is a surface mounted four-pole machine with one slot per pole and phase (q = 1).

6.2.1 Initial stator geometry

The initial properties of the stator geometry are set by optimizing the machine with respect to the copper losses. In addition to the constraints listed in 6.1.1 the following restrictions are set:

- magnet thickness $h_m = 3{,}5$ mm
- airgap length $\delta = 0{,}75$ mm

The copper losses are minimized for the following stator geometry.

Active length L [mm]	55,0
Outer stator diameter D_y [mm]	90,0
Inner stator diameter D [mm]	41,2
Stator slot height h_{ss} [mm]	17,4
Stator yoke height h_{sy} [mm]	7,0
Inner stator slot width b_{ss1} [mm]	6,3
Outer stator slot width b_{ss2} [mm]	14,7
Stator tooth width b_{ts} [mm]	5,2
Stator slot wedge height h_{sw} [mm]	1,5
Stator slot opening/slot width k_{open} [%]	0,3
Stator slot pitch τ_s [mm]	10,8
Circumferential magnet width w_m [mm]	20,8

Table 6-1 Dimensions used for the stator

These are the stator dimensions that are used during the parameter study regarding the airgap length in 6.2.2 and the magnet thickness in 6.2.3.

6.2.2 Influence of the airgap length

In this section the influence of the airgap length δ is studied. In order to obtain comparable results the stator dimensions are the same for all values of δ. Instead the rotor core diameter is changed in such a way that it compensate a change of the airgap length. The magnet thickness h_m is kept constant equal to 3,5 mm. The current loading is changed so that the same torque is obtained.
The machine performance at different airgap lengths are summarised in Table 6-2.

Airgap length δ [mm]	1,0	0,75	0,50
Rotor core diameter D_{rc} [mm]	32,2	32,7	33,2
Efficiency η [%]	93,2	93,8	94,2
Displacement power factor $\cos\varphi$ [1]	0,92	0,93	0,94
Peak phase current $\hat{I}$ [A]	17,3	17,2	16,5
Copper losses P_{cu} [W]	304	263	225
Iron losses P_{iron} [W]	72	82	94
End-winding temp. $T_{endwind}$ [^{o}C]	112	102	93
Magnet temp. T_{mag} [^{o}C]	66	63	61

Table 6-2 Influence of the airgap length

As expected, a small airgap length gives a higher efficieny. This is due to an increased fundamental airgap flux density. The iron losses slightly increase with a decreased airgap length. But the copper losses and the winding temperature decrease quite much.
Notice that the airgap length can not be too small when a bandage is required. The bandage thickness h_{band} is expected to be approximately 0,2 mm. The actual mechanical airgap length is given by:

$$\delta_{mech} = \delta - h_{band} \qquad \textbf{(6-28)}$$

But a mechanical airgap of 0,3 mm is possible. The experimental PMSM machine used by Lindström in [11] had an outer rotor diameter of 117 mm and a mechanical airgap of 0,3 mm. In this case the rotor diameter is much smaller, thus the thermal expansion of the rotor is smaller.

[1] Note that the influence of the end-winding inductance not is taken into account.

Influence of the magnet thickness

The airgap length δ is now set constant and equal to 0,5 mm. The stator dimensions are kept the same. The influence of the magnet thickness h_m is studied. Table 6-3 shows the influence on the performance when the magnet thickness is varied.

Magnet thickness h_m [mm]	2,50	2,75	3,00	3,25	3,50
Rotor core diameter D_{rc} [mm]	35,2	34,7	34,2	33,7	33,2
Efficiency η [%]	93,8	94,0	94,1	94,1	94,2
Displacement power factor $\cos\varphi$ [1]	0,90	0,91	0,93	0,94	0,94
Peak phase current $\hat{I}$ [A]	17,5	17,2	16,9	16,7	16,5
Copper losses P_{cu} [W]	251	243	236	230	225
Iron losses P_{iron} [W]	91	92	92	93	94
End-winding temperature $T_{endwind}$ [^{o}C]	100	97	96	94	93
Magnet temperature T_{mag} [^{o}C]	63	62	62	61	61
Magnet mass M_{mag} [g]	81	90	96	104	111

Table 6-3 Influence of the magnet thickness

The characteristics of the results are similar to the results obtained when the airgap length is varied. Although the deviation of the results at different magnet thicknesses are not that large. The magnet material is very expensive, thus the magnet thickness directly influences the manufacturing cost. A thicker magnet also requires thicker bandage. This increases the total magnetic airgap which limits the output power of the machine. On the other hand, the magnets are very brittle so a thin magnet makes the manufacturing process more complicated. A magnet thickness of 3,25 mm seems reasonable.

6.2.3 Influence of the rotor diameter

The rotor core diameter D_{rc} is varied. For each rotor diameter, an optimization is performed with respect to the copper losses. This gives an optimum stator geometry for each rotor diameter (optimum in terms of minimized copper losses). The optimization is performed with the constraints listed in 6.1.1. And in each iteration the rotor core diameter is treated as a fixed value. In addition to these constraints the following restrictions are set:

- magnet thickness h_m = 3,25 mm
- airgap length δ = 0,5 mm

The rotor diameter influences the losses, the temperatures in the motor and the weight of the machine is studied. Figure 6-4 and Figure 6-5 shows the copper losses and the iron losses as a function of the rotor diameter.

[1] Note that the influence of the end-winding inductance not is taken into account.

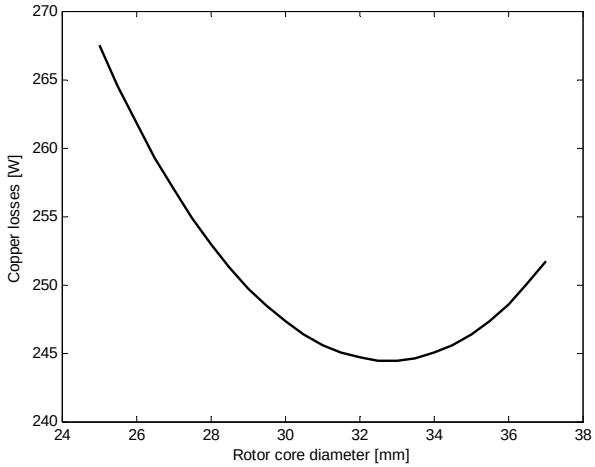

Figure 6-4 Influence on the copper losses

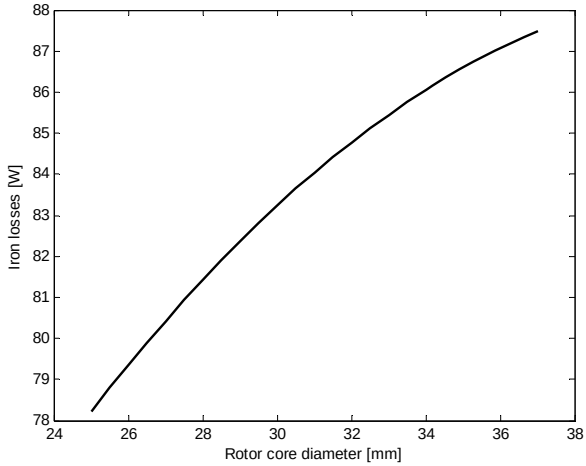

Figure 6-5 Influence on the iron losses

One can see that it exists rotor diameter that minimizes the copper losses. But to the cost of a slightly higher amount of iron losses. The iron losses are easier to deal with in a thermal point of view. They are situated closer to the coolant than the copper losses. Therefore the iron losses contribute less to a high operating temperature than the copper losses.

In a thermal point of view, the end-windings and the magnets are the most important parts of the machine. The highest temperature appears in the end-winding and the magnets are sensitive to high temperatures. These temperatures are shown in Figure 6-6 and Figure 6-7.

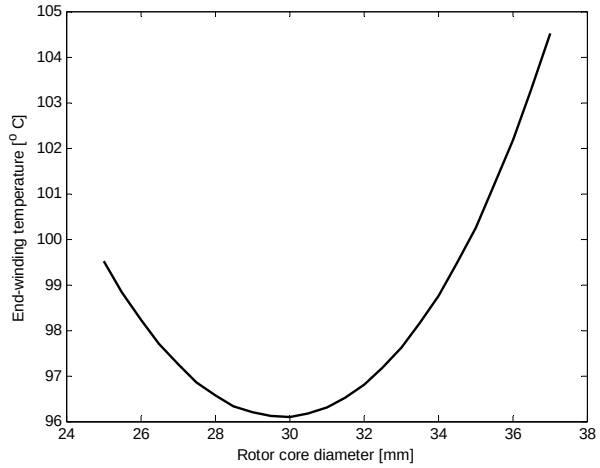

Figure 6-6
Influence on the End-winding temperature

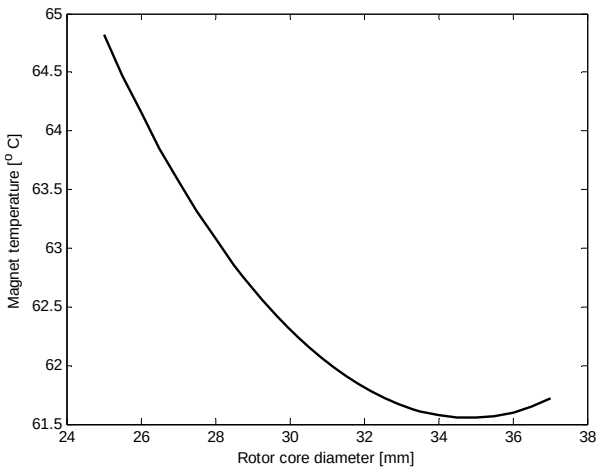

Figure 6-7
Influence on the magnet temperature

These results from the thermal model should taken with care as many assumptions have been made. However, the results seem to be quite reasonable. It can be seen that the end-winding temperature varies similarly as the copper losses, although the rotor core diameters at their minimum points slightly differ. This is due to the fact that the stator geometry is different for each rotor diameter, and this also affects the thermal resistances in the different parts of the machine.

The magnet mass and the total mass of the electromagnetic parts of the machine are shown in Figure 6-8 and Figure 6-9 respectively.

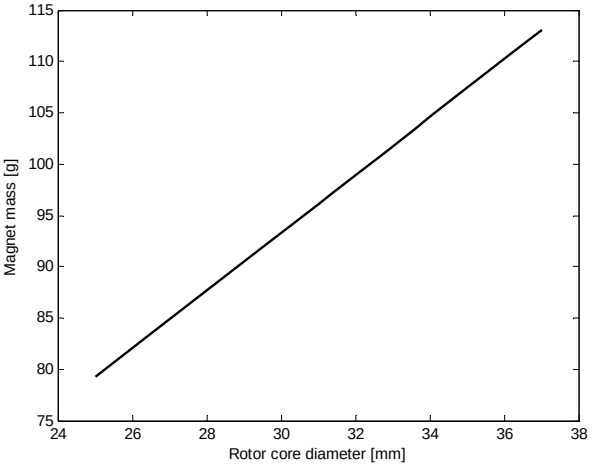

Figure 6-8 Influence on magnet mass

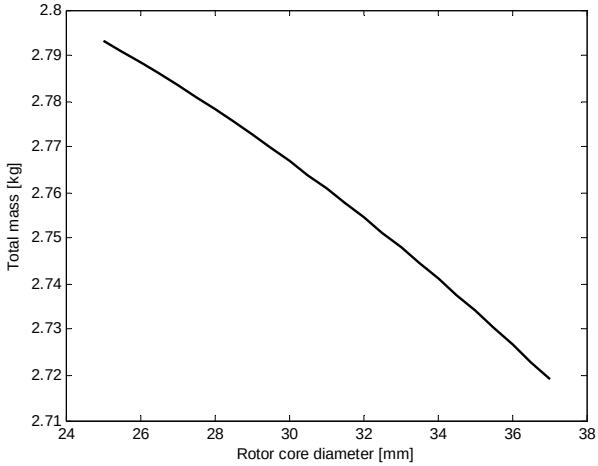

Figure 6-9 Influence on total mass of the electromagnetic parts of the motor

The total mass of the machine is quite unaffected for this relatively small change of the rotor core diameter. The weight of the electromagnetic parts of the machine seems to be approximately 60 % of the maximum allowed weight. The weight of the aluminium frame is estimated to approximately 0,25 kg. This gives a total motor weight of approximately 3 kg.

6.3 The prototype machine

This section presents the suggested prototype machine. The design that resulted in the lowest amount of copper losses in section 6.2.4 is presented thoroughly here.

6.3.1 Dimensions

The geometry achieved from the optimization procedure is slightly modified. This due to the unreasonably high accuracy of the parameters obtained from the optimization. Therefore the results may vary somewhat compared to the curves in the previous section. Figure 6-10 shows a cross section of the machine.

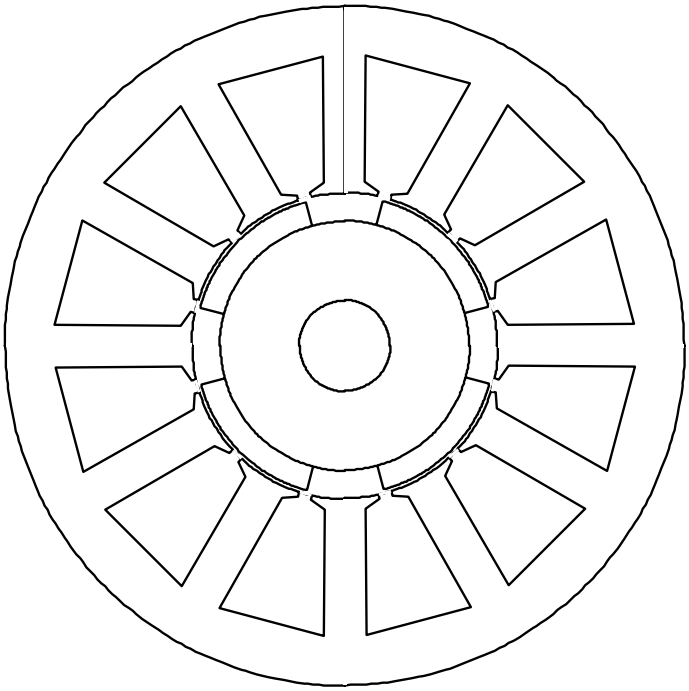

Figure 6-10 The prototype machine in scale 1:1

All geometrical dimensions corresponding to Figure 6-1 and Figure 6-2 are listed in Table 6-4.

Active length L [mm]	55,0
Outer stator diameter D_y [mm]	90,0
Inner stator diameter D [mm]	40,5
Rotor core diameter D_{rc} [mm]	33,0
Shaft diameter D_i [mm]	12,0
Height of rotor back h_{ry} [mm]	10,5
Airgap δ [mm]	0,5
Magnet thickness h_m [mm]	3,25
Circumferential magnet width w_m [mm]	20,7
Stator slot pitch τ_s [mm]	10,6
Stator slot height h_{ss} [mm]	17,6
Stator yoke height h_{sy} [mm]	7,2
Inner stator slot width b_{ss1} [mm]	5,9
Outer stator slot width b_{ss2} [mm]	14,3
Stator tooth width b_{ts} [mm]	5,5
Slot wedge height h_{sw} [mm]	1,3
Stator slot opening/slot width k_{open} [%]	0,3

Table 6-4 Dimensions of the prototype machine

The stator frame is suggested to be made as described in 4.1.1 with the following dimensions:

- a = 7 mm
- b = 2 mm
- c = 1 mm

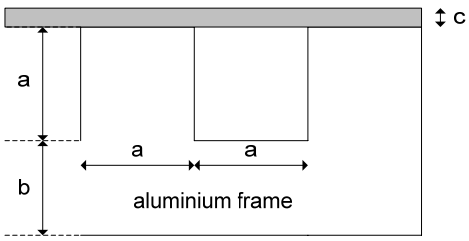

Figure 6-11 Stator frame geometry

6.3.2 Stator winding

The investigated winding is a distributed winding with q = 1 and with the conductors connected in series. The number of conductors per slot is: $n_s = 54$. The conductor diameter is 1,32 mm. This gives a current density of 8,8 A/mm^2. The resistance of one phase winding is given by: $R_{cu} = 560\ \text{m}\Omega$. These calculations are made under the assumption that it is possible to obtain a slot fill factor of $f_s = 0{,}5$.

6.3.3 Materials

The iron lamination used for the calculations are M400-50A manufactured by Cogent Power Ltd at Surahammars Bruks AB in Sweden. This is as a middle range quality of lamination with a thickness of 0,5 mm. Aluminium has thermal properties well suited for the stator frame. NdFeB is probably the best magnetic material for this application. A sintered magnet is preferred when a high remanence flux density is required. The calculations are performed with a remanence flux density of 1,08 T. With a magnet temperature of approximately 60^o C and assuming a reversible temperature coefficient $\alpha_{B_r} = -0{,}0012\,K^{-1}$ [14], the required remanence flux density at 25^o C is: $B_r(25^o\,C) = 1{,}13$ T according to Equation (2-3).

6.3.4 Performance

The analytical calculated performance of the motor are listed in Table 6-5. Verification of these results is made with Flux2D in chapter 7.

Rated speed N_n [rpm]	10 000
Rated torque T_n [Nm]	5,5
Rated power S_n [kVA]	6,5
Efficiency η [%]	94,1
Displacement power factor $\cos\varphi$ [1]	0,94
Peak phase current $\hat{i}$ [A]	16,9
Copper losses P_{cu} [W]	241
Iron losses P_{iron} [W]	87
End-winding temp. $T_{endwind}$ [^{o}C]	96
Magnet temp. T_{mag} [^{o}C]	62
Magnet mass M_{mag} [hg]	1,0
Total mass (including frame) M_{tot} [kg]	3,0

Table 6-5 Performance of the prototype machine

[1] Note that the influence of the end-winding inductance not is taken into account.

The thermal model described in chapter 4 gives the following temperature distribution in machine.

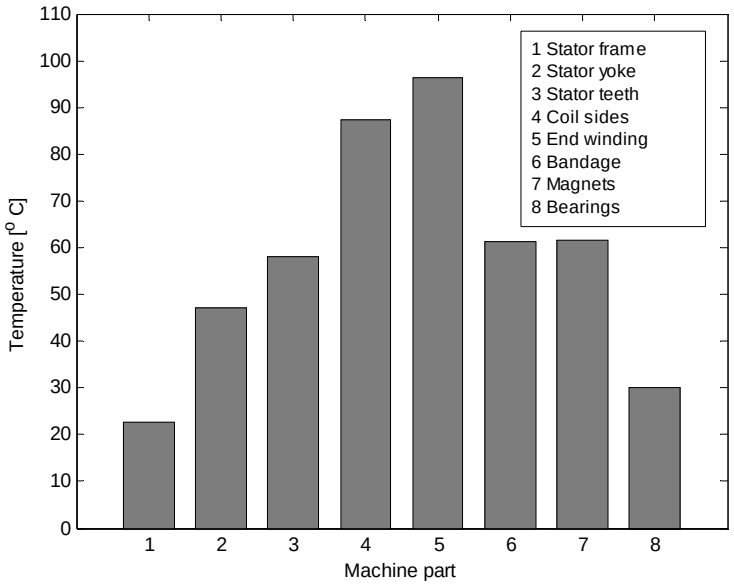

Figure 6-12 Temperature distribution

It can be seen that the highest temperature appears in the End-winding. This temperature is mostly depending on the thermal resistance between the coil sides and the stator teeth. It is of importance to keep this resistance as low as possible with the intention to avoid overheating.
Another critical parameter is the coolant temperature. All the machine temperatures are directly influenced by this value as the model calculates the temperature rises in reference to the average coolant temperature. With the loss models used in this thesis, the temperatures seem to be acceptable with an average coolant temperature of 22,5 ^{o}C and a minimum coolant flow of approximately 1 litre/min.

6.3.5 Bandage requirements

The procedure described in section 2.3.1 is used to determine the minimum bandage thickness.
If a 0,2 mm thick bandage consisting of 60% glass-fibre and 40% epoxy is used, the residual pressure becomes:

$$p_{res} = 2{,}5 \ N/mm^2 \ \ (> 0 \text{ required}) \qquad \textbf{(6-29)}$$

This guarantees that the magnets will not leave the rotor surface. The maximum tangential strength becomes:

$$\sigma_{\max} = 390 \ N/mm^2 \ \ (< 600 \text{ required}) \qquad \textbf{(6-30)}$$

which ensures that the bandage does not burst. In the above calculations, it is assumed that the inner diameter of the prefabricated glass fiber bandage cylinder is smaller than the rotor outer diameter d, by the value $\Delta d = 0{,}3 \ mm$.

$$d = D_{rc} + 2h_m \qquad \textbf{(6-31)}$$

With the suggested bandage thickness $h_{band} = 0{,}2\,\text{mm}$, the mechanical airgap δ_{mech} becomes 0,3 mm.

7 Verification with FEM

Flux2D is the software used for the finite element method. The results are used to verify the analytical calculations. This chapter describes the basic setup in the program and simulation results are presented.

7.1 Basic setup

The machine geometry is exported from Matlab into Flux2D via an .spi file. In Flux 2D, the different machine parts are assigned a specific material. In a magnetic simulation, the non-magnetic materials are represented by vacuum. The magnet material is created in order to describe the required remanence flux density. The suggested iron material is available in the material database.

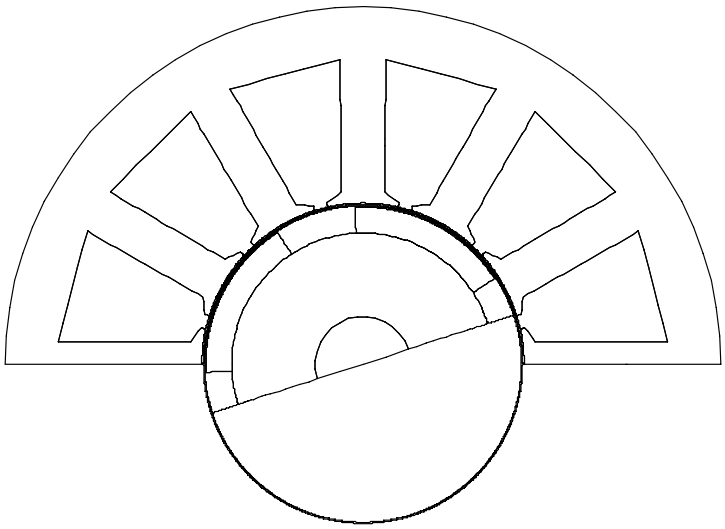

Figure 7-1 FEM geometry of the motor (one half of the motor is drawn only)

Two types of simulations are made:

- magneto-static, used for calculation of the flux density created by the magnets
- transient magnetic, used for calculations of the torque and the iron losses at rated speed

For the transient magnetic simulation, a circuit is used in order to impose the rated currents. This circuit is shown in Figure 7-2.

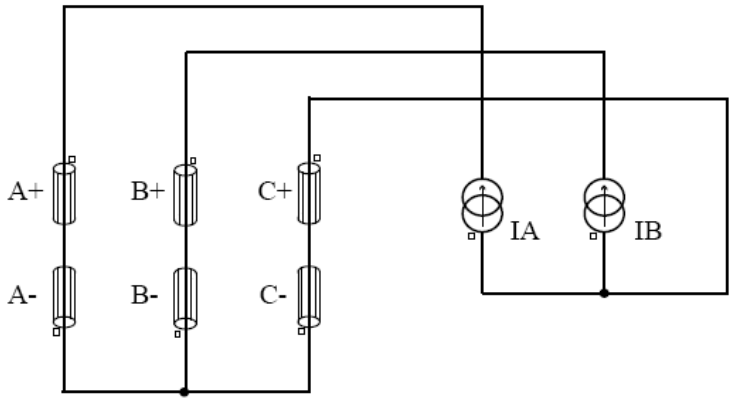

Figure 7-2 Electrical circuit with load

The current sources are assigned the stator current peak value calculated in section 6.1.4. Further on, a sinusoidal variation is used and the current sources are phase shifted by 120 degrees. The coils A+ and A- represent one slot of the positive and the negative phase A and contain the number of conductors per slot n_s. The resistance of each coil is calculated from the phase resistance R_{cu} which represents the total resistance of one phase. The coil resistances are therefore given by the phase resistance divided by the pole number. Note that this is valid only for this specific winding arrangement.

7.2 Results

This section presents the results obtained by the static and the transient magnetic simulations.

7.2.1 Verification of the airgap flux density

A static simulation is made in order to validate the analytical calculation of the airgap flux density. Figure 7-3 shows the normal component of the airgap flux density created by the magnets in one half of the machine. The respective spectrum analysis is shown in Figure 7-4.

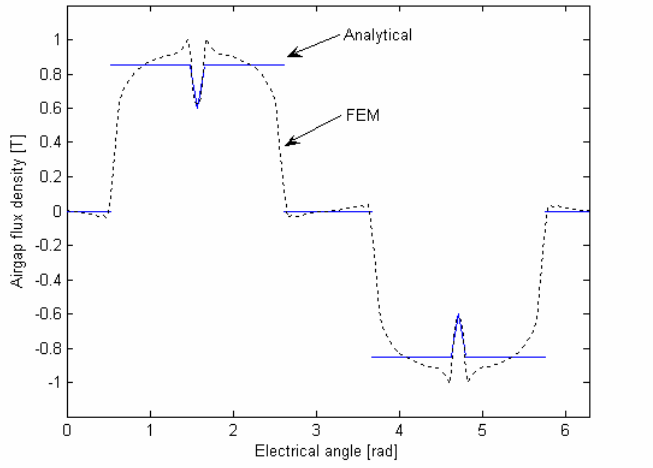

Figure 7-3
Airgap flux density created by the magnets

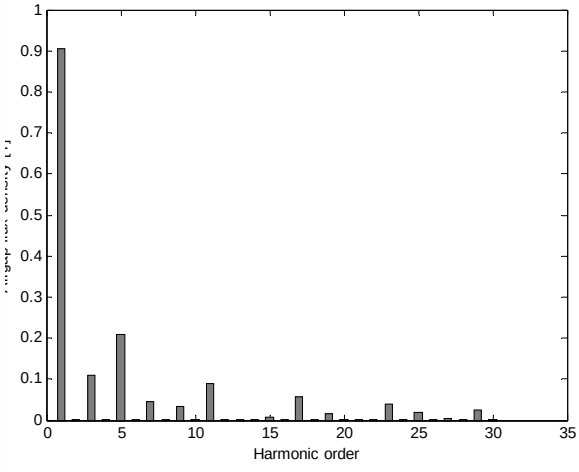

Figure 7-4
Harmonic content

The fundamental component of the airgp flux density obtained by the FEM calculations is 0,91 T. The corresponding analytical value is 0,92 T. One can see that it exists a third harmonic, although its magnitude should be suppressed due to the choice of the pole angle. But its magnitude is larger than expected, probably due to the relatively small airgap. The resulting airgap flux density created by the magnets and the currents at rated speed and torque is shown in Figure 7-5. The actual airgap flux density is distorted due to the armature reaction.

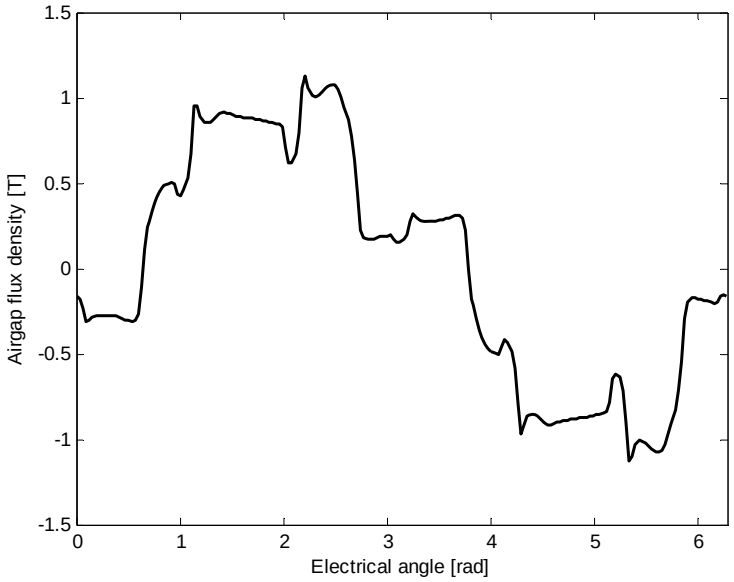

Figure 7-5 Resulting airgap flux density at nominal load

7.2.2 Verification of the iron losses

The machine is simulated at rated speed and torque. The FEM model is used to calculate the iron losses in the stator and the rotor core. The analytical model of the stator core losses seems to be reliable. The results obtained by the analytical model used during the design process and the FEM calculations are presented in Table 7-1. As expected, the rotor core losses are very small.

	Stator core losses	Rotor core losses	Flux density in stator teeth $\hat{B}_{st}$	Flux density in stator yoke $\hat{B}_{sy}$
Analytical	87 W	-	~1,6 T	~1,4 T
FEM	91 W	< 1 W	~1,7 T	~1,5 T

Table 7-1 Iron loss comparison

7.2.3 Verification of the axis torque

The analytical calculations are performed in order obtain an axis torque of approximately 5,5 Nm. The axis torque obtained by the FEM calculations is shown in Figure 7-6.

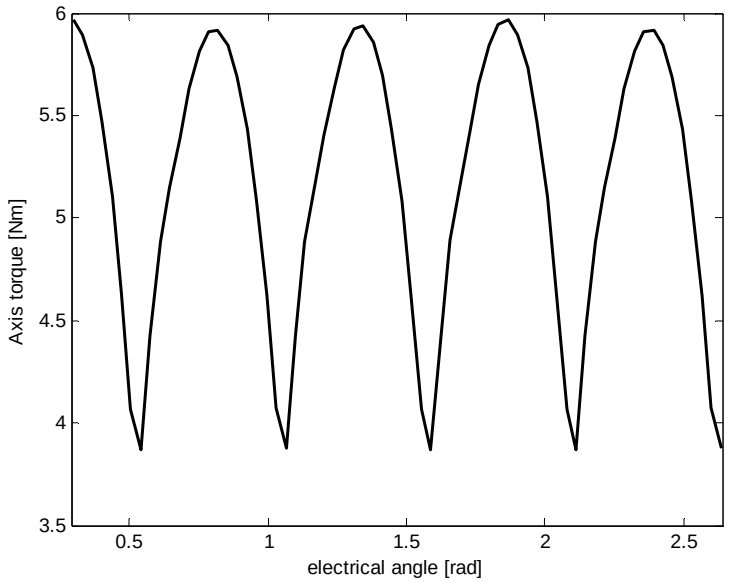

Figure 7-6 Axis torque

The mean value of this axis torque is 5,2 Nm which is 5,5 % lower than the analytical value. This is partly due to the reduced airgap flux density created by the magnets (-1,8 %) and also due to the slot leakage that reduces the current loading in the airgap.

8 Conclusions and future work

The purpose with this thesis was to design and optimize a permanent magnet synchronous motor for an industrial cutter. Some choices have been made in order to restrict the extension of the work. A SMPM motor with a concentrated winding was expected to fulfil the requirements. It is a simple motor concept and it is relatively easy to manufacture. As Florence Libert already developed a design program for this motor type, the thesis work was focused on this concept. Further on, the machine design was restricted to a four pole machine with one slot per pole and phase. The four pole concept was chosen partly due to the high rotational speed and partly due to the required torque. A higher pole number requires a higher stator frequency, leading to increased iron losses as well as increased switching losses. Due to the limited space for the stator winding, one slot per pole and phase is probably the most suitable solution for the four pole machine.

Models for the different losses in the machine have been developed and implemented into the design program. In addition to the copper losses, iron losses as well as bearing losses and windage losses are considered. Special attention was given to the development of a thermal model used to predict temperatures in different parts of the motor. A stator frame with a helicoidal coolant duct was designed in order to tackle the expected amount of losses.
A basic drive system for the motor has been described, possible requirements on the power factor were also considered. Attention was also given to the modelling of the mechanical stresses on the magnets, leading to requirements of the bandage.

According to the used analytical models, the suggested machine design fulfils the requirements. This was also confirmed with finite element method simulations. The results showed acceptable correlation between the two methods. The iron losses formed a significant fraction of the total motor losses, approximately 25 %. The bearing losses and the windage losses were small for this motor design, but these models could be useful when designing larger or faster machines.
It is possible to operate the motor at a higher winding temperature than the winding temperature obtained from the thermal model of the prototype motor. However, a lot of assumptions were made in this model. The manufacturing technique being unknown, it is probably unwise to design the motor for a higher operating temperature. The duty cycle for the motor is also unknown. All calculations were made under steady-state conditions, but further investigations of the thermal behavior should be conducted once the duty cycle for the motor is better described.
The main components of the motor drive seemed to be well suited for the application. It was also possible to reduce the harmonic content in the grid current in order to achieve a higher power factor. Regarding the magnet fixation, the glass-fibre bandage should be strong enough if it is manufactured correctly.

An interesting future work could be to study the influence of a concentrated winding. As the machine is short, it is of interest to reduce the required space for the end-windings. This is obtained with a concentrated winding. But the number of poles and the number of slots have to be chosen with care for this winding arrangement, otherwise the torque ripple and the rotor losses could be high.
Regarding the thermal model, if measurements are made on a prototype machine, the theoretical model could be compared and developed further. A possible method is also to do a comparison with thermal finite element method simulations.

There is remaining work on the motor drive. Specific components for the rectifier and the inverter should be chosen and the DC-capacitance should be calculated. The control strategy has to be determined as well.
Calculations can also be made on a carbon-fibre bandage, which probably results in a thinner bandage. The increase of rotor losses if a thin non-magnetic steel cylinder was used instead of a glass-fibre bandage could be investigated in Flux2D.

This work was the first stage of the motor drive designs and many other aspects can be investigated more thoroughly. Many question marks will probably also find some answers by building and testing the first prototype.

References

[1] C. Sadarangani, *Electrical Machines – Design and Analysis of Induction and Permanent Magnet Motors,* ISBN 91-7170-627-5, KTH Högskoletryckeriet, Stockholm, 2000.

[2] Ch. Schätzer, A. Binder, *Design Optimization of a High-Speed Permanent Magnet Machine with the VEKOPT Algorithm,* Industry Applications Conference, 2000, Conference Record of the IEEE, Volume 1, 8-12 Oct. 2000, Page(s):439 – 444 vol.1.

[3] Florence Libert, *Design, Optimization and Comparison of Permanent Magnet Motors for a Low-Speed Direct-Driven Mixer,* Licentiate Thesis, KTH Department of Electrical Engineering Electrical Machines and Power Electronics, ISBN 91-7283-901-5, Stockholm 2004.

[4] Slemon, G.R., Bonert, R. and Mi, C. *Modeling of Iron Losses of Surface-Mounted Permanent Magnet Synchronous Motors,* Conference Record of the IEEE IAS Annual Meeting, Volume 4, 30 Sept.-4 Oct. 2001 Page(s):2585 - 2591 vol.4.

[5] J. Saari, *Thermal Analysis of High-speed Induction Machines,* Acta Polytechnica Scandinavica, Electrical Engineering Series No. 90. Helsinki 1998. Published by the Finnish Academy of Technology. ISBN 952-5148-43-2. ISSN 0001-6845. UDC 621.313.

[6] Ragulskis,Yurkauskas, *Vibration of bearings,* ISBN 0-89116-829-X, Hemisphere Publishing Corporation, 1989.

[7] www.skf.com

[8] B. Kuttner, *Dubbel Handbook of Mechanical Engineering,* ISBN 3-540-19868-7, Springer-Verlag London Limited, 1994.

[9] F. Kreith, S. Bohn, *Principles of Heat Transfer, Fourth Edition*, ISBN 0-06-043774-X, Harper International Edition ISBN 0-06-350388-3, 1986.

[10] Mohan, Undeland, Robbins, *Power electronics, converters, applications, and design,* ISBN 0-471-58408-8, John Wiley & Sons, 1995.

[11] J. Lindström, *Development of an Experimental Permanent-Magnet Motor Drive,* Licentiate thesis, Technical Report No. 312L, Chalmers University of Technology, 1999.

[12] P.H. Mellor, D. Roberts, D.R. Turner, *Lumped parameter thermal model for electrical machines of TEFC design,* IEE Proceedings B, Electric Power Applications, Volume 138, Issue 5, Sept. 1991 Page(s): 205 – 218.

[13] S. Meier, *Theoretical design of surface-mounted permanent magnet motors with field-weakening capability.* Master Thesis, KTH Department of Electrical Engineering Electrical Machines and Power Electronics, Stockholm 2002.

[14] www.suramagnets.se

List of symbols and abbreviations

List of abbreviations

AC	alternating current
DC	direct current
FEM	finite element method
IM	induction motor
PM	permanent magnet
SMPM	surface-mounted permanent magnet

List of symbols

A	area	$[m^2]$
A_{cu}	copper area per slot	$[m^2]$
A_{sl}	stator slot area	$[m^2]$
a	stator frame tooth height	[m]
B	magnetic flux density	[T]
B_d	demagnetisation flux density	[T]
B_m	maximum value of the magnetic flux density in the airgap above the magnets	[T]
B_r	magnetic remanence flux density	[T]
$\hat{B}_{ry}$	maximum flux density in rotor yoke	[T]
$\hat{B}_{st}$	maximum flux density in stator teeth	[T]
$\hat{B}_{sy}$	maximum flux density in stator yoke	[T]
$\hat{B}_{\delta}$	maximum fundamental airgap flux density	[T]
b	stator frame yoke height	[m]
b_{ss1}	inner stator slot width	[m]
b_{ss2}	outer stator slot width	[m]
b_{ts}	stator tooth width	[m]
C_f	friction coefficient	[-]
C_{p_c}	specific heat capacity of the coolant	[J/kg/K]
c	stator frame coverage thickness	[m]
$\cos(\varphi)$	displacement power factor	[-]
cov	magnet coverage	[-]
D	inner stator diameter	[m]
D_i	shaft diameter	[m]
D_{rc}	rotor core diameter	[m]
D_y	outer stator diameter	[m]
d	outer rotor diameter	[m]

d_{ins}	slot insulation thickness	[m]
d_{air}	equivalent airgap for modelling of the coil contact resistance	[m]
d_{lam}	lamination thickness	[m]
E	induced phase voltage	[V]
E_B	Youngs's modulus	[N/mm^2]
F_b	bearing load	[N]
F_r	tangential friction force acting on the rotor surface	[N]
f	frequency	[Hz]
f_s	stator slot fill factor	[-]
g_e	equivalent airgap for modelling of the thermal contact resistance	[m]
H	magnetic field strength	[A/m]
H_{cJ}	permanent magnet coercivity	[A/m]
h_b	bandage thickness	[m]
h_c	convective heat transfer coefficient	[W/K/m^2]
$\overline{h}_c$	average value of the convective heat transfer coefficient	[W/K/m^2]
h_{fr}	average height of the stator frame	[m]
h_m	magnet thickness	[m]
h_{ry}	height of rotor back	[m]
h_{ss}	stator slot height	[m]
h_{sy}	stator yoke height	[m]
h_{sw}	slot wedge height	[m]
I	rms-value of the stator current	[A]
I_d	DC-link current	[A]
$\hat{I}_{max}$	maximum allowed peak value of the stator current	[A]
I_s	rms line current	[A]
I_{sc}	line short circuit current	[A]
I_{s1}	rms line current at the fundamental frequency	[A]
$\hat{I}_1$	maximum value of the stator current at the fundamental frequency	[A]
$\hat{J}$	maximum conductor current density	[A/m^2]
k_B	Stefan Boltzmann constant	[W/m^2/K^4]
k_b	bearing torque coefficient	[m]
k_C	Carter factor	[-]
k_c	geometry dependent correction factor	[-]
k_{coil}	end-winding coefficient	[-]
k_{cu}	thermal conductivity of copper	[W/K/m]
k_e	eddy current loss coefficient	[Ws^2/T^2/m^3]
k_{exc}	excess loss coefficient	[Ws$^{3/2}$/T$^{3/2}$/m^3]
k_{Fe}	iron stacking factor	[-]
k_f	roughness coefficient	[-]

k_h	hysteresis loss coefficient	[Ws/T^2/m^3]
k_{hyst}	FEM hysteresis loss coefficient	[Ws/T^2/m^3]
k_{ins}	thermal conductivity of the slot insulation	[W/K/m]
k_k	thermal conductivity	[W/K/m]
k_{leak}	correction factor for the airgap flux density calculation	[-]
k_{open}	ratio of the slot opening over the slot width	[-]
k_{open}	stator slot opening/slot width	[-]
k_q	geometry dependent correction factor	[-]
$k_{winding}$	equivalent thermal conductivity of the winding	[W/K/m]
k_{w1}	fundamental winding factor	[-]
L	active machine length	[m]
L_d	d-axis inductance	[H]
L_l	stator leakage inductance	[H]
L_m	magnetising inductance	[H]
L_q	q-axis inductance	[H]
L_s	smoothing inductance	[H]
l_{av}	average length of half a turn of the winding coil	[m]
l_{Fe}	stator core length	[m]
l_{use}	useful iron lenth	[m]
M_{mag}	total magnet mass	[kg]
M_{tot}	active weight of the machine	[kg]
m_a	amplitude modulation ratio	[-]
N_n	nominal speed	[rpm]
N_s	number of turns per phase	[-]
n_s	number of conductors per stator slot	[-]
p	number of poles	[-]
p_{bb}	centrifugal pressure of the bandage	[N/mm^2]
p_{bm}	pressure of the bandage on the magnets	[N/mm^2]
P_{cu}	copper losses	[W]
p_e	eddy current loss density	[W/ m^3]
p_{e_teeth}	stator teeth eddy current loss density	[W/ m^3]
p_{e_yoke}	stator yoke eddy current loss density	[W/ m^3]
PF	power factor	[-]
P_{f_b}	total bearing loss	[W]
P_{f_r}	airgap windage loss	[W]
p_h	hysteresis loss density	[W/ m^3]
p_{h_teeth}	stator teeth hysteresis loss density	[W/ m^3]
p_{h_yoke}	stator yoke hysteresis loss density	[W/ m^3]
P_{in}	inverter input power	[W]
p_{iron}	total iron loss density	[W/ m^3]

P_{loss_stator}	total stator iron loss	[W]
P_{loss}	total motor losses	[W]
P_{motor}	electrical power of the motor	[W]
p_{mb}	centrifugal pressure of the magnets on the bandage	[N/mm^2]
p_{res}	residual pressure on the bandage	[N/mm^2]
p_{teeth}	total stator teeth loss density	[W/ m^3]
p_{yoke}	total stator yoke loss density	[W/ m^3]
R_c	convective thermal resistance	[K/W]
R_{cu}	winding resistance of one phase	[Ω]
Re_δ	Couette Reynolds number	[-]
R_k	conductive thermal resistance	[K/W]
r_b	average radius of the bandage	[m]
r_m	average radius of the magnets	[m]
r_r	rotor outer radius	[m]
t	time	[s]
S	apparent power	[VA]
S_n	rated power	[VA]
S_l	sinusoidal stator current loading	[A/m]
T	temperature	[K]
T	torque	[Nm]
T_{f_b}	bearing friction torque	[Nm]
T_{f_r}	rotor surface friction torque	[Nm]
T_n	nominal torque	[Nm]
T_0	load independent torque	[Nm]
T_l	load dependent torque	[Nm]
U_d	average value of the output voltage from a three phase diode rectifier	[V]
U_{d_0}	average value of the output voltage from an ideal three phase diode rectifier	[V]
U_{LL_1}	inverter output line-to-line rms voltage at the fundamental frequency	[V]
U_1	rms phase voltage at the fundamental frequency	[V]
u	grid phase voltage	[V]
u_d	DC-link voltage	[V]
V	voltage	[V]
v_{min}	minimum coolant speed	[m/s]
v_r	rotor peripheral speed	[m/s]
Q_{min}	minimum coolant flow	[m^3/s]
q	number of slots per pole and phase	[-]
q_c	heat flow by convection	[W]
q_k	heat flow by conduction	[W]
q_r	heat flow by radiation	[W]
q_s	total number of stator slots	[-]

x	distance	[m]
Z_L	grid impedance	[Ω]
w_m	circumferential magnet width	[m]
α	half pole angle	[rad]
α_{B_r}	reversible temperature coefficient	[K^{-1}]
β	electrical angle between the current and the magnet flux vector	[rad]
β_{St}	Steinmetz constant	[-]
δ	airgap length without bandage	[m]
δ_{mech}	mechanical airgap length	[m]
η	efficiency	[-]
$\eta_{inverter}$	inverter efficiency	[-]
η_{motor}	motor efficiency	[-]
$\eta_{rectifier}$	rectifier efficiency	[-]
λ_1	specific permeance coefficient of the slot opening	[-]
μ	dynamic viscosity	[Ns/m^2]
μ_0	magnetic permeability of free space	[H/m]
μ_f	bearing friction coefficient	[-]
μ_r	relative magnet permeability	[H/m]
Φ_m	fundamental magnet flux	[Vs]
Ψ_m	magnet flux linkage	[Vs]
ρ	mass density	[kg/ m^3]
ρ_c	coolant mass density	[kg/ m^3]
ρ_{cu}	resistivity of copper	[Ωm]
ρ_m	magnet mass density	[kg/m^3]
ρ_b	bandage mass density	[kg/m^3]
σ	tension	[N/mm^2]
σ_{iron}	lamination conductivity	[$(\Omega m)^{-1}$]
σ_{max}	maximum tangential strength	[N/mm^2]
τ_p	pole pitch	[m]
τ_r	shear stress on the rotor surface	[N/m^2]
τ_s	stator slot pitch	[m]
τ_{s2}	projected slot pitch at the middle of the stator yoke	[m]
ω	angular velocity	[rad/s]
ω_e	electrical angular velocity	[rad/s]
ω_m	mechanical angular velocity	[rad/s]
ω_{over}	bandage dimensioning speed	[rad/s]

Appendix A

More information regarding the following equations can be found in [11].

Definition of the thermal resistances

R_{th1} – thermal resistance between frame and coolant

R_{th2} – thermal resistance between frame and stator yoke

R_{th3} – thermal resistance between stator yoke and stator teeth

R_{th4} – thermal resistance between stator teeth and coil sides

R_{th5} – thermal resistance between coil sides and end winding

R_{th6} – thermal resistance between stator teeth and rotor sleeve surface

R_{th7} – thermal resistance between rotor sleeve surface and magnets

R_{th8} – thermal resistance between magnets and bearings

R_{th9} – thermal resistance between bearings and frame

R_{th10} – thermal resistance between stator teeth and magnets

R_{th11} – thermal resistance between magnets and frame

R_{th12} – thermal resistance between magnets and end winding

R_{th13} – thermal resistance between end winding and frame

Calculation of the thermal resistances

The thermal resistances are calculated from the equivalent conduction and convection resistances of the different parts of the motor.

$$R_{th1} = \frac{1}{2} R_{th\_fr}$$

$$R_{th2} = \frac{1}{2}\left(R_{th\_fr} + R_{th\_ys}\right) + R_{th\_cy}$$

$$R_{th3} = \frac{1}{2}\left(R_{th\_d} + R_{th\_ys}\right)$$

$$R_{th4} = \frac{R_x R_y}{q_s l_{use}(R_x + R_y)}\left(1 - \frac{R_{x0} R_{y0}}{720(R_{xo} + R_{y0})}\right)$$

$$R_{th5} = \frac{R_{th\_w}}{2q_s}$$

$$R_{th6} = R_{th\_\delta} + \frac{1}{2}R_{th\_d}$$

$$R_{th7} = R_{th\_sl} + \frac{1}{2}R_{th\_pm}$$

$$R_{th8} = \frac{1}{2}R_{th\_pm} + R_{th\_ins} + R_{th\_yr} + R_{th\_cr} + \frac{1}{2}R_{th\_sh} + \frac{1}{4}R_{th\_b}$$

$$R_{th9} = \frac{1}{4}R_{th\_b}$$

$$R_{th10} = R_{th6} + R_{th7}$$

$$R_{th11} = \frac{R_1R_3 + R_2R_3 + R_2R_1}{R_3}$$

$$R_{th12} = \frac{R_1R_3 + R_2R_3 + R_2R_1}{R_1}$$

$$R_{th13} = \frac{R_1R_3 + R_2R_3 + R_2R_1}{R_2}$$

Definition of the equivalent conduction and convection resistances

R_{th_fr} – radial thermal resistance of the frame

R_{th_ys} – radial thermal resistance of the stator yoke

R_{th_cy} – contact resistance between frame and stator yoke

R_{th_d} – radial thermal resistance of the stator teeth

R_x – tangential component of the resistance of the slot material in per unit – length

R_y – radial component of the resistance of the slot material in per unit – length

R_{th_w} – thermal resistance from the mid point of the end winding to the mid point of the coil side

R_1 – convective thermal resistance between internal air and frame

R_2 – convective thermal resistance between internal air and rotor

R_3 – convective thermal resistance between internal air and end winding

R_{th_δ} – thermal resistance of the air gap between rotor and stator

R_{th_yr} – radial rotor yoke thermal resistance

R_{th_pm} – thermal resistance of the magnets

R_{th_sl} – radial thermal resistance of the rotor sleeve

R_{th_ins} – thermal resistance of the magnet insulation

R_{th_sh} – axial thermal resistance of the shaft

R_{th_b} – thermal resistance of one bearing

R_{th_cr} – contact resistance between rotor core and shaft

Calculation of the equivalent conduction and convection resistances

$$R_{th\_fr} = \frac{h_{fr}}{\pi l_{Fe} k_{Al} (D_y + h_{fr})}$$

$$R_{th\_ys} = \frac{\ln\left(\frac{D_y}{2}\right) - \ln\left(\frac{D_y}{2} + h_{ss}\right)}{2\pi l_{use} k_{Fe}}$$

$$R_{th\_cy} = \frac{g_e}{k_{air} \pi D_y l_{use}}$$

$$R_{th\_d} = \frac{h_{ss}}{k_{Fe} q_s l_{use} b_{ts}}$$

$$R_x = \frac{1}{2}\left(R_{ix} + \frac{R_{x0}}{6}\right)$$

$$R_y = \frac{1}{2}\left(R_{iy} + \frac{R_{y0}}{6}\right)$$

$$R_{x0} = \frac{\frac{1}{2}(b_{ss1} + b_{ss2}) - 2(d_{ins} + d_{air})}{k_{winding}\left(\frac{2A_{sl}}{b_{ss1} + b_{ss2}} - 2(d_{ins} + d_{air})\right)}$$

$$R_{y0} = \frac{\frac{2A_{sl}}{b_{ss1} + b_{ss2}} - 2(d_{ins} + d_{air})}{k_{winding}\left(\frac{1}{2}(b_{ss1} + b_{ss2}) - 2(d_{ins} + d_{air})\right)}$$

$$R_{ix} = \left(\frac{d_{ins}}{k_{ins}} + \frac{d_{air}}{k_{air}}\right)\frac{1}{\frac{2A_{sl}}{b_{ss1} + b_{ss2}} - 2(d_{ins} + d_{air})}$$

$$R_{iy} = \left(\frac{d_{ins}}{k_{ins}} + \frac{d_{air}}{k_{air}} \right) \frac{1}{\frac{1}{2}(b_{ss1} + b_{ss2}) - 2(d_{ins} + d_{air})}$$

$$R_{th\_w} = \frac{l_{av}}{3 A_{cu} k_{cu}}$$

$$R_1 = \frac{1}{(15 + 6{,}75^{0{,}65} + v_r^{0{,}65}) \left(2\pi \frac{(D_{rc}^2 - D_i^2)}{4} + \pi D_{rc} l_{use} \right)}$$

$R_2 = \text{not defined, more information can be found in } [11]$

$$R_3 = \frac{1}{(6{,}5 + 5{,}25^{0{,}65} v\_r^{0{,}6}) \pi (l_{av} - l_{use})(D + 0{,}5 h_{ss})}$$

$$R_{th\_\delta} = \frac{1}{\alpha_\delta \pi D L}, \text{ where } \alpha_\delta = \frac{Nu\, k_{air}}{2\delta}$$

$$\text{Nusslet number : } Nu = 0{,}409\, Ta^{0{,}241} - 137\, Ta^{-0{,}75}$$

$$\text{Taylor number : } Ta = \frac{\omega_m^2 D \delta^3}{2 \mu_{air}}$$

$$R_{th\_yr} = \frac{\ln\left(\frac{D_{rc}}{2}\right) - \ln\left(\frac{D_i}{2}\right)}{2\pi l_{use} k_{Fe}}$$

$$R_{th\_pm} = \frac{\pi}{2\alpha} \left(\frac{\ln\left(\frac{D_{rc}}{2} + h_m\right) - \ln\left(\frac{D_{rc}}{2}\right)}{2\pi l_{Fe} k_{pm}} \right)$$

$$R_{th\_sl} = \frac{\frac{\pi}{2\alpha} h_{band}}{\pi (D_{rc} + 2h_m) l_{Fe} k_{band}}$$

$$R_{th\_ins} = \frac{\frac{\pi}{2\alpha} d_{ins}}{\pi D_{rc} l_{Fe} k_{ins}}$$

$$R_{th\_sh} = \frac{4L}{\pi D_i^2 k_{sh}}$$

$$R_{th\_b} = 0{,}45(0{,}12 - 2D_i)33$$

$$R_{th\_cr} = \frac{g_e}{\pi D_i l_{use} k_{air}}$$

Appendix B

Optimization procedure

The followed procedure to optimize the design of PM motors [3].